

Coupling a three-dimensional subsurface flow and transport model with a land surface model to simulate stream-aquifer-land interactions (CPv1.0) [MS No.: gmd-2017-35]

Responses to review comments

Topical Editor Decision: Reconsider after major revisions (21 Sep 2017) by Jatin Kala
Comments to the Author:

Dear authors,

Apologies for the delay, a second review never came back. I have reviewed your responses, but i remain unconvinced about the reasons you outline for not comparing CPv1.0 fluxes with CLM stand alone fluxes. These are of course different models, making different assumptions. But this is not a valid reason for not explaining the differences. You simply refer the reader to Figure S4, and leave the reader to make their own conclusions. The differences in latent heat flux between CPv1.0 and CLM stand alone are very large. You need to explain why these differences are so large. And which is likely to be more "correct/realistic"???

If you were to use CLM versus CPv1.0 coupled to an atmospheric model, such large differences in latent heat flux would have a very large influence on near surface temperature, humidity, boundary-layer structure etc. I do not think you can leave this analysis out. You have added/coupled an additional component to CLM, it makes sense to me, that you should compare simulations with the additional component, to the original model. That would generally be expected for any model development. A reader of this manuscript will be left very confused as to why the latent heat fluxes are so different between the two. You have to address this explicitly in the manuscript.

Kind regards,

Jatin

[Response:](#)

Dear Editor,

Thank you very much for your suggestions. We greatly appreciate your effort. We agree with your comments that it is important to show the difference between CP v1.0 and CLM to illustrate how model assumptions would affect the simulations, and provide explanations to mechanisms leading to such differences.

In response to your comments, we made the following changes in the revised manuscript:

- Two new figures are added:
 - Figure 12 that compares spatially-averaged key hydrologic fluxes and states simulated by CLM and CPv1.0 for the study period.
 - Figure S9 that shows spatial maps of CLM4.5 simulated latent heat flux for the month of June during the study period, and their differences from that of S_{2m} .
- Differences in simulation results of CLM and CP v1.0 are discussed in the revised manuscript in sections 4.2 and 5 on pages 18, 19, and 22.

- Additionally, corresponding changes are made to the abstract (page 2) and section 3.2 (page 15).

We sincerely hope that our revisions are satisfactory so that the manuscript can be accepted for publication. Thanks again and we look forward to hearing from you.

Maoyi on behalf of the co-authors

1 **Coupling a three-dimensional subsurface flow and transport**
2 **model with a land surface model to simulate stream-aquifer-**
3 **land interactions (CP v1.0)**

4

5 | Gautam Bisht¹, Maoyi Huang^{2,*}, Tian Zhou², Xingyuan Chen², Heng Dai², Glenn [E. Hammond](#)³,
6 | William [J. Riley](#)¹, Janelle [L. Downs](#)², Ying Liu², John [M. Zachara](#)²

7

8 ¹Lawrence Berkeley National Laboratory, Berkeley, CA

9 ²Pacific Northwest National Laboratory, Richland, WA

10 ³Sandia National Laboratories, Albuquerque, NM

11

12

13 Correspondence to: Maoyi Huang (maoyi.huang@pnnl.gov)

14

15

16 Revised Manuscript to be considered for *Geoscientific Model Development*

17

18 **Abstract**

19 A fully coupled three-dimensional surface and subsurface land model is developed and applied
20 to a site along the Columbia River to simulate three-way interactions among river water,
21 groundwater, and land surface processes. The model features the coupling of the Community
22 Land Model version 4.5 (CLM4.5) and a massively-parallel multi-physics reactive transport
23 model (PFLOTRAN). The coupled model, named CP v1.0, is applied to a 400 m × 400 m study
24 domain instrumented with groundwater monitoring wells along the Columbia River shoreline.
25 CP v1.0 simulations are performed at three spatial resolutions (i.e., 2 m, 10 m, and 20 m) over a
26 five-year period to evaluate the impact of hydro-climatic conditions and spatial resolution on
27 simulated variables. Results show that the coupled model is capable of simulating groundwater-
28 river water interactions driven by river stage variability along managed river reaches, which are
29 of global significance as a result of over 30,000 dams constructed worldwide during the past half
30 century. Our numerical experiments suggest that the land-surface energy partitioning is strongly
31 modulated by groundwater-river water interactions through expanding the periodically inundated
32 fraction of the riparian zone, and enhancing moisture availability in the vadose zone via capillary
33 rise in response to the river stage change. [Meanwhile, CLM4.5 fails to capture the key](#)
34 [hydrologic process \(i.e., groundwater-river water exchange\) at the site, and consequently](#)
35 [simulates drastically different water and energy budgets.](#) Furthermore, spatial resolution is found
36 to impact significantly the accuracy of estimated the mass exchange rates at the boundaries of the
37 aquifer, and it becomes critical when surface and subsurface become more tightly coupled with
38 groundwater table within six to seven meters below the surface. Inclusion of lateral subsurface
39 flow influenced both the surface energy budget and subsurface transport processes as a result of
40 river water intrusion into the subsurface in response to elevated river stage that increased soil
41 moisture for evapotranspiration and suppressed available energy for sensible heat in the warm
42 season. The coupled model developed in this study can be used for improving mechanistic
43 understanding of ecosystem functioning and biogeochemical cycling along river corridors under
44 historical and future hydro-climatic changes. The dataset presented in this study can also serve as
45 a good benchmarking case for testing other integrated models.

46

47 **1 Introduction**

48 Previous modeling studies have demonstrated that subsurface hydrologic model structure and
49 parameterization can significantly affect simulated land-atmosphere exchanges [*Condon et al.*,
50 2013; *Hou et al.*, 2012; *Kollet and Maxwell*, 2008; *Miguez-Macho and Fan*, 2012] and therefore
51 boundary layer dynamics [*Maxwell and Miller*, 2005; *Rihani et al.*, 2015], cloud formation
52 [*Rahman et al.*, 2015], and climate [*Leung et al.*, 2011; *Taylor et al.*, 2013]. Lateral subsurface
53 processes are fundamentally important at multiple spatial scales, including hill-slope scales
54 [*McNamara et al.*, 2005; *Zhang et al.*, 2011], basin scales in semi-arid and arid climates where
55 regional aquifers sustain baseflows in rivers [*Schaller and Fan*, 2009], and wetlands [*Fan and*
56 *Miguez-Macho*, 2011]. However, some current-generation land surface models (LSMs) routinely
57 omit explicit lateral subsurface processes [*Clark et al.*, 2015; *Kollet and Maxwell*, 2008; *Nir et*
58 *al.*, 2014], while others include them (described below). Observational and modeling studies
59 suggest that groundwater forms an environmental gradient in soil moisture availability by
60 redistributing water that could profoundly shape critical zone evolution at continental to global
61 scales [*Fan et al.*, 2013; *Taylor et al.*, 2013]. The mismatch between observed and simulated
62 evapotranspiration by current LSMs could be explained by the absence of lateral groundwater
63 flow [*Maxwell and Condon*, 2016].

64 It has been increasingly recognized that rivers, despite their small aerial extent on the
65 landscape, play important roles in watershed functioning through their connections with
66 groundwater aquifers and riparian zones [*Shen et al.*, 2016]. The interactions between
67 groundwater and river water prolong physical storage and enhance reactive processing that alter
68 water chemistry, downstream transport of materials and energy, and biogenic gas emissions
69 [*Fischer et al.*, 2005; *Harvey and Gooseff*, 2015]. The Earth System modeling community
70 recognizes such a gap in existing Earth system models and calls for improved representation of
71 biophysical and biogeochemical processes within the terrestrial-aquatic interface [*Gaillardet et*
72 *al.*, 2014].

73 Over the past decade, much effort has been expended to include groundwater into LSMs.
74 Groundwater is important to water and energy budgets such as evapotranspiration (ET), latent
75 heat (LH), and sensible heat (SH), but also to biogeochemical processes such as gross primary
76 production, heterotrophic respiration, and nutrient cycling. The lateral convergence of water
77 along the landscape and two-way groundwater-surface water exchange are identified as the most

78 relevant subsurface processes to large-scale Earth System functioning (see review by *Clark et al.*
79 [2015]). However, the choice of processes, the approaches to represent multi-scale structures and
80 heterogeneities, the data and computational demands, etc., all vary greatly among the research
81 groups even working on the same land models.

82 Most of the LSMs reviewed by *Clark et al.* [2015] do not explicitly account for stream-
83 aquifer-land interactions. For example, the Community Land Model version 4.5 allows for
84 reinfiltration of flooded waters in a highly parameterized way without explicitly linking to
85 groundwater dynamics, therefore only one-way flow from the aquifer to the stream is simulated
86 [*Oleson et al.*, 2013]. The Land-Ecosystem-Atmosphere Feedback model treats river elevation as
87 part of the 2-D vertically integrated groundwater flow equation and allows river and floodwater
88 to infiltrate through sediments in the flood plain [*Miguez-Macho and Fan*, 2012].

89 In contrast, the fully integrated models, being a small subset of LSMs, explicitly represent
90 the two-way exchange between groundwater aquifers and their adjacent rivers in a spatially
91 resolved fashion. Such models couple a completely integrated hydrology model with a land
92 surface model, so that the surface-water recharge to groundwater by infiltration or intrusion and
93 base flow discharge from groundwater to surface waters can be estimated in a more mechanistic
94 way.

95 Examples of the integrated models include: (1) the coupling between the Common Land
96 Model (CoLM) and a variably saturated groundwater model (ParFlow) [*Maxwell and Miller*,
97 2005]; (2) the Penn State Integrated Hydrologic Model (PIHM) [*Shi et al.*, 2013]; (3) the
98 coupling between the Process-based Adaptive Watershed Simulator (PAWS) and CLM4.5 [*Ji et*
99 *al.*, 2015; *Pau et al.*, 2016; *Riley and Shen*, 2014]; (4) the coupling between the CATchment
100 Hydrology (CATHY) model and the Noah model with multiple parameterization schemes
101 (Noah-MP) [*Niu et al.*, 2014]; and (5) the coupling between CLM3.5 and ParFlow through the
102 Ocean Atmosphere Sea Ice Soil external coupler (OASIS3) in the Terrestrial Systems Modeling
103 Platform (TerrSysMP) [*Shrestha et al.*, 2014; *Gebler et al.*, 2017]. The integrated models
104 eliminate the need for parameterizing lateral groundwater flow and allow the interconnected
105 groundwater–surface-water systems to evolve dynamically based on the governing equations and
106 the properties of the physical system. Although such models often require robust numerical
107 solvers on high-performance computing (HPC) facilities to achieve high-resolution, large-extent
108 simulations [*Maxwell et al.*, 2015], they have been increasingly applied for hydrologic prediction

109 and environmental understanding. However, as a result of difference in physical process
110 representations and numerical solution approaches in terms of (1) the coupling between the
111 variably saturated groundwater and surface water flow; (2) representation of surface water flow;
112 and (3) implementation of subsurface heterogeneity in the existing integrated models,
113 significant discrepancies exist in their results when the models were applied to highly nonlinear
114 problems with heterogeneity and complex water table dynamics, while many of the models show
115 good agreement for simpler test cases where traditional runoff generation mechanisms (i.e.,
116 saturation and infiltration excess runoff) apply [Kollet *et al.*, 2017; Maxwell *et al.*, 2014].

117 The developments of the integrated models have enabled scientific explorations of
118 interactions and feedback mechanisms in the aquifer-soil-vegetation-atmosphere continuum
119 using a holistic and physically based approach [Shrestha *et al.*, 2014; Gilbert *et al.*, 2017].
120 Compared to simulations of regional climate models coupled to traditional LSMs, such a
121 physically based approach shows less sensitivity to uncertainty in the subsurface hydraulic
122 characteristics that could propagate from deep subsurface to free troposphere [Keune *et al.*,
123 2016], while other physical representations (e.g., parameterizations in evaporation and
124 transpiration, atmospheric boundary layer schemes) could have significant effects on the
125 simulations as well [Sulis *et al.*, 2017]. Therefore, it is of great scientific interest to further
126 develop the integrated models and benchmarks to achieve improved understanding of complex
127 interactions in the fully coupled Earth system.

128 Motivated by the great potentials of using an integrated model to explore Earth system
129 dynamics, the objective of this study is three-fold. First, we aim to document the development of
130 a coupled land surface and subsurface model as a first step toward a new integrated model,
131 featuring the two-way coupling between two highly-scalable and state-of-the-art open-source
132 codes: CLM4.5 [Oleson *et al.*, 2013] and a reactive transport model PFLOTRAN [Lichtner *et al.*,
133 2015]. The coupled model mechanistically represents the two-way exchange of water and solute
134 mass between aquifers and river, as well as land-atmosphere exchange of water and energy. The
135 coupled model is therefore named as CP v1.0 hereafter. We note that in recent years, efforts have
136 been made to implement carbon–nitrogen decomposition, nitrification, denitrification, and plant
137 uptake from CLM4.5 in the form of a reaction network solved by PFLOTRAN to enable the
138 coupling of biogeochemical processes between the two models [Tang *et al.*, 2016]. In addition,
139 although PAWS is coupled to the same version of CLM (i.e., CLM4.5) [Ji *et al.*, 2015; Pau *et*

140 *al.*, 2016], PFLOTRAN resolves the subsurface in a 3-D fashion, while PAWS approximates the
141 3D Richards equation by divide the subsurface into an unsaturated domain represented by the 1-
142 D Richards Equation coupled with 3D saturated groundwater flow equation for subsurface flow,
143 by assuming that there is no horizontal flow in unsaturated portion of soil, and that lateral flux in
144 saturated portion is evenly distributed.

145 Second, we describe a numerically challenging benchmarking case for verifying coupled land
146 surface and subsurface models, featuring a highly dynamic river boundary condition determined
147 by dam-induced river stage variations (Hauer et al., 2017), representative of managed river
148 reaches that are of global significance as a result of dam constructions in the past few decades
149 [Zhou et al., 2016]. Third, we assess the effects of spatial resolution and projected hydro-climatic
150 changes on simulated land surface fluxes and exchange of groundwater and river water using the
151 coupled model and datasets from the benchmarking case. In section 2, we describe the
152 component models and our coupling strategy. In section 3, we describe an application of the
153 model to a field site along the Hanford reach of the Columbia River, where the subsurface
154 properties are well characterized and long-term monitoring of river stage, groundwater table, and
155 exchange of groundwater and river water exist. In section 4, we assess the effects of spatial
156 resolution and hydro-climatic conditions to simulated fluxes and state variables. In section 5,
157 conclusion and future work are discussed.

158

159 **2 Model description**

160 **2.1 The Community Land Model version 4.5**

161 CLM4.5 [Oleson et al., 2013] is the land component of the Community Earth System Model
162 version 1 (CESM1) [Hurrell et al., 2013], a fully coupled numerical simulator of the Earth
163 system consisting of atmospheric, ocean, ice, land surface, carbon cycle, and other components.
164 It has been applied successfully to explore interactions among water, energy, carbon, and
165 biogeochemical cycling at local to global scales [Leng et al., 2016b; Xu et al., 2016], and proven
166 to be highly scalable on leading HPC facilities such as the U.S. Department of Energy
167 (USDOE)'s National Energy Research Scientific Computing Center (NERSC). The model
168 includes parameterizations of terrestrial hydrological processes including interception,
169 throughfall, canopy drip, snow accumulation and melt, water transfer between snow layers,

170 infiltration, evaporation, surface runoff, sub-surface drainage, redistribution within the soil
171 column, and groundwater discharge and recharge to simulate changes in canopy water, surface
172 water, snow water, soil water, and soil ice, and water in the unconfined aquifer [Oleson *et al.*,
173 2013]. Precipitation is either intercepted by the canopy, falls directly to the snow/soil surface
174 (throughfall), or drips off the vegetation (canopy drip). Water input at the land surface, the sum
175 of liquid precipitation reaching the ground and melt water from snow, is partitioned into surface
176 runoff, surface water storage, and infiltration into the soil. Two sets of runoff generation
177 parameterizations, including formulations for saturation and infiltration excess runoff and
178 baseflow, are implemented into the model: the TOPMODEL-based runoff generation
179 formulations [Beven and Kirkby, 1979; Niu *et al.*, 2005; Niu *et al.*, 2007] and the Variable
180 Infiltration Capacity (VIC)-based runoff generation formulations [Lei *et al.*, 2014; Liang *et al.*,
181 1994; Wood *et al.*, 1992]. Surface water storage and outflow in and from wetlands and small sub-
182 grid scale water bodies are parameterized as functions of fine-spatial-scale elevation variations
183 called microtopography. Soil water is predicted from a multi-layer model based on the 1-D
184 Richards equation, with boundary conditions and source/sink terms specified as infiltration,
185 surface and sub-surface runoff, gradient diffusion, gravity, canopy transpiration through root
186 extraction, and interactions with groundwater. A groundwater component is added in the form of
187 an unconfined aquifer lying below the soil column following Niu *et al.* [2007]. The model
188 computes surface energy fluxes following the Monin-Obukhov Similarity Theory using
189 formulations in Zeng *et al.* (1998), which updates the calculation of boundary resistance to
190 account for understory turbulence, sparse and dense canopies, and surface litter layer (Sakaguchi
191 and Zeng, 2009; Zeng *et al.*, 2005; Zeng and Wang, 2007). Water and energy budgets are
192 conserved at every modeling step.

193 **2.2 PFLOTRAN**

194 PFLOTRAN is a massively-parallel multi-physics simulator [Hammond *et al.*, 2014] developed
195 and distributed under an open source GNU LGPL license and is freely available through
196 Bitbucket ((<https://bitbucket.org/pflotran/pflotran>)). It solves a system of generally nonlinear
197 partial differential equations (PDEs) describing multiphase, multicomponent and multiscale
198 reactive flow and transport in porous materials. The PDEs are spatially discretized using a finite
199 volume technique, and the backward Euler scheme is used for implicit time discretization. It has

200 been widely used for simulating subsurface multiphase flow and reactive biogeochemical
 201 transport processes [*Chen et al.*, 2013; *Chen et al.*, 2012; *Hammond and Lichtner*, 2010;
 202 *Hammond et al.*, 2011; *Kumar et al.*, 2016; *Lichtner and Hammond*, 2012; *Liu et al.*, 2016; *Pau*
 203 *et al.*, 2014]

204 PFLOTRAN is written in object-oriented Fortran 2003/2008 and relies on the PETSc
 205 framework [*Balay et al.*, 2015] to provide the underlying parallel data structures and solvers for
 206 scalable high performance computing. PFLOTRAN uses domain decomposition and MPI
 207 libraries for parallelization. PFLOTRAN has been run on problems composed of over 3 billion
 208 degrees of freedom with up to 262,144 processors, but it is more commonly employed on
 209 problems with millions to tens of millions of degrees of freedom utilizing hundreds to thousands
 210 of processors. Although PFLOTRAN is designed for massively parallel computation, the same
 211 code base can be run on a single processor without recompiling, which may limit problem size
 212 based on available memory.

213 In this study, PFLOTRAN is used to simulate single phase variably saturated flow and solute
 214 transport in the subsurface. Single-phase variably saturated flow is based on the Richards
 215 equation with the form

$$216 \quad \frac{\partial}{\partial t}(\varphi s \rho) + \nabla \cdot \rho \mathbf{q} = 0, \quad (1)$$

217 with liquid density ρ , porosity φ , and saturation s . The Darcy velocity, \mathbf{q} , is given by

$$218 \quad \mathbf{q} = -\frac{k k_r}{\mu} \nabla(p - \rho g z), \quad (2)$$

219 with liquid pressure p , viscosity μ , acceleration of gravity g , intrinsic permeability k , relative
 220 permeability k_r and elevation above a given datum z . Conservative solute transport in the liquid
 221 phase is based on the advection-dispersion equation

$$222 \quad \frac{\partial}{\partial t}(\varphi s C) + \nabla \cdot (\mathbf{q} - \varphi s D \nabla) C = 0, \quad (3)$$

223 with solute concentration C and hydrodynamic dispersion coefficient D . The discrete system of
 224 nonlinear PDEs for flow and transport are solved using the Newton-Raphson method.

225 **2.3 Model coupling**

226 In this study, CLM4.5's one-dimensional models for flow in unsaturated [Zeng and Decker,
227 2009] and saturated [Niu et al., 2007] zones are replaced by PFLOTRAN's RICHARDS mode to
228 simulate unsaturated-saturated flow within the three-dimensional subsurface domain. Although
229 PFLOTRAN is also capable of simulating coupled flow and thermal processes in the subsurface
230 including explicit representation of liquid-ice phase [Karra et al., 2014], as well as, soil nutrient
231 cycles [Hammond and Lichtner, 2010; Zachara et al., 2016; Tang et al., 2016], those processes
232 are not coupled between the two models in this study. A schematic representation of the coupling
233 between CLM4.5 and PFLOTRAN is shown in Figure 1. A model coupling interface based on
234 PETSc data structures was developed to couple the two models and the interface includes some
235 key design features of the CESM coupler [Craig et al., 2012]. The model coupling interface
236 allows each model grid to have a different spatial resolution and domain decomposition across
237 multiple processors. While CLM4.5 uses a round-robin decomposition approach, PFLOTRAN
238 employs domain decomposition via PETSc (Figure 1a). Interpolation of gridded data from one
239 model onto the grids of the other is done through sparse matrix vector multiplication. As a
240 preprocessing step, sparse weight matrices for interpolating data between the two models are
241 saved as mapping files. Analogous to the CESM coupler, the mapping files are saved in a format
242 similar to the mapping files produced by the ESMF_RegridWeightGen
243 (<https://www.earthsystemcog.org/projects/regridweightgen>). ESMF regriding tools provide
244 multiple interpolation methods (conservative, bilinear, and nearest neighbor) to generate the
245 sparse weight matrix.

246 In this work, we have used a conservative remapping method to interpolate data between
247 CLM and PFLOTRAN. During model initialization, the model coupling interface first
248 collectively reads all required sparse matrices. Next, the model coupling interface reassembles
249 local sparse matrices after accounting for domain decomposition of each model (figures 1b and
250 1c). . For a given time step, CLM4.5 first computes infiltration, evaporation, and transpiration
251 within the domain and then sends the data to the model coupling interface. The model coupling
252 interface for each processor receives relevant CLM data vector from all other processors;
253 interpolates data from CLM's grid onto PFLOTRAN's grid via a local sparse matrix vector
254 multiplication; and saves the resulting vector in PFLOTRAN's data structures as prescribed flow
255 conditions (Figure 1b). PFLOTRAN evolves the subsurface states over the given time step

256 length. The updated soil moisture simulated by PFLOTRAN are then provided back to the model
257 coupling interface, which interpolates data from PFLOTRAN's grid onto CLM's grid (Figure
258 1c). The interpolated data is saved in CLM4.5's data structure and used for simulating land
259 water- and energy- budget terms in the next step. Figure 2 shows a schematic representation of
260 how stream-aquifer-land interactions are simulated in CP v1.0 when applied to the field scale,
261 such as the 300 Area domain to be introduced in section 3.1.

262

263 **3 Site description and model configuration**

264 **3.1 The Hanford site and the 300 Area**

265 The Hanford Reach is a stretch of the lower Columbia River extending approximately 55 km
266 from the Priest Rapids hydroelectric dam to the outskirts of Richland, Washington, USA (Figure
267 3a) [Tiffan *et al.*, 2002]. The Columbia River above Priest Rapids Dam drains primarily
268 mountainous regions in Canada, Idaho, Montana, and Washington, over which spatio-temporal
269 distributions of precipitation and snowmelt modulate the timing and magnitude of river flows
270 [Elsner *et al.*, 2010; Hamlet and Lettenmaier, 1999]. The Columbia River is highly regulated by
271 dams for power generation and river stage and discharge along the Hanford Reach displays
272 significant variation on multiple time scales. Strong seasonal variations occur with the greatest
273 discharge (up to $12,000 \text{ m}^3 \text{ s}^{-1}$) occurring from May through July due to snow melt, with less
274 discharge ($>1,700 \text{ m}^3 \text{ s}^{-1}$) and lower flows occurring in the fall and winter [Hamlet and
275 Lettenmaier, 1999; Waichler *et al.*, 2005]. Significant variation in discharge also occurs on a
276 daily or hourly basis due to power generation, with fluctuations in river stage of up to 2 m within
277 a 6-24 hr period being common [Tiffan *et al.*, 2002].

278 The Hanford site features an unconfined aquifer developed in Miocene-Pliocene fluvial and
279 lacustrine sediments of the Ringold Formation, overlain by Pleistocene flood gravels of the
280 Hanford formation [Thorne *et al.*, 2006] that is in hydrologic continuity with the Columbia
281 River. The Hanford formation gravel and sand, deposited by glacial outburst floods at the end of
282 the Pleistocene [Bjornstad, 2007], has a high average hydraulic conductivity at $\sim 3,100 \text{ m day}^{-1}$
283 [Williams *et al.*, 2008]. The fluvial deposits of the Ringold Formation have much lower
284 hydraulic conductivity than the Hanford but are still relatively conductive at 36 m day^{-1}

285 [Williams *et al.*, 2008]. Fine-grained lacustrine Ringold silt has a much lower estimated
286 hydraulic conductivity of 1 m day^{-1} . The hydraulic conductivity of recent alluvium lining the
287 river channel is low relative to the Hanford formation, which tends to dampen the response of
288 water table elevation in wells near the river when changes occur in river stage [Hammond *et al.*,
289 2011; Williams *et al.*, 2008]. Overall, the Columbia River through the Hanford Reach is a prime
290 example of a hyporheic corridor with an extensive floodplain aquifer. It is consequently an ideal
291 alluvial system for evaluating the capability of the coupled model in simulating stream-aquifer-
292 land interactions.

293 The region is situated in a cold desert climate with temperatures, precipitation, and winds that
294 are greatly affected by the presence of mountain barriers. The Cascade Range to the west creates
295 a strong rain shadow effect by forming a barrier to moist air moving from the Pacific Ocean,
296 while the Rocky Mountains and ranges to the north protect it from the more severe cold polar air
297 masses and winter storms moving south across Canada. Meteorological data are collected by the
298 Hanford Meteorological Monitoring Network (<http://www.hanford.gov/page.cfm/hms>), which
299 collects meteorological data representative of the general climatic conditions for the Hanford
300 site.

301 A segment of the hyporheic corridor in the Hanford 300 Area (300A) was chosen to evaluate
302 the model's capability in simulating river-aquifer-land interactions. Located at the downstream
303 end of the Hanford Reach, the impact of dam operations on river stage is relatively damped,
304 exhibiting a typical variation of $\sim 0.5 \text{ m}$ within a day and 2-3 m in a year. The study domain
305 covers an area of $400 \text{ m} \times 400 \text{ m}$ along the Columbia River shoreline (Figure 3b). Aquifer
306 sediments in the 300 Area are coarse grained and highly permeable [Chen *et al.*, 2013;
307 Hammond and Lichtner, 2010]. Coupled with dynamic river stage variations, the resulting
308 system is characterized by stage-driven intrusion and retreat of river water into the adjacent
309 unconfined aquifer system. During high-stage spring runoff events, river water has been detected
310 in monitoring wells nearly 400 m from the shoreline [Williams *et al.*, 2008]. During baseline,
311 low-stage conditions (October-February), the Columbia River is a gaining stream, and the
312 aquifer pore space is occupied by groundwater.

313 The study domain is instrumented with groundwater monitoring wells (Figure 3b) and a river
314 gaging station that records water table elevations. A vegetation survey in 2015 was conducted to
315 provide aerial coverages of grassland, shrubland, riparian trees in the domain (Figure 3b). A

316 high-resolution topography and bathymetry dataset at 1-m resolution was assembled from
317 multiple surveys by *Coleman et al.* [2010]. The data layers originated from Deep Water
318 Bathymetric Boat surveys, terrestrial Light Detection and Ranging (LiDAR) surveys, and special
319 hydrographic LiDAR surveys penetrating through water to collect both topographic and
320 bathymetric elevation data.

321 **3.2 Model configuration, numerical experiments, and analyses**

322 To assess the effect of spatial resolution on simulated variables such as latent heat, sensible heat,
323 water table depth, and river water in the domain, we configured CP v1.0 simulations at three
324 horizontal spatial resolutions: 2-m, 10-m, and 20-m over the 400 m×400 m domain, respectively.
325 For comparison purposes, we also configured a 2-m-resolution CP v1.0 vertical only simulation
326 (i.e., S_{v2m}) in which lateral transfers of flow and solutes in the subsurface are disabled. Due to
327 lack of observations of water and energy fluxes from the land surface, in this study we treat the
328 2-m-resolution CP v1.0 as the baseline and compare simulation results at other resolutions to it.
329 New hydrologic regimes are projected to emerge over the Pacific Northwest in as early as the
330 2030s due to increases in winter precipitation and earlier snow melt in response to future
331 warming [*Leng et al.*, 2016a]. Therefore, we expect that spring and early summer river discharge
332 along the reach might increase in the future. To evaluate how land surface-subsurface coupling
333 might be modulated hydro-climatic conditions, we designed additional numerical experiments by
334 driving the model with elevated river stages by adding five meters to the observed river stage
335 time series. The simulations and their configurations are summarized in Table 1.

336 The PFLOTRAN subsurface domain, also terrain-following and extending from soil surface
337 (including riverbed) to 32 m below the surface, was discretized using a structured approach with
338 rectangular grids. For the 2-m, 10-m, and 20-m resolution simulations, each mesh element was 2
339 m × 2 m, 10 m × 10 m, and 20 m×20 m, in the horizontal direction, and 0.5 m in the vertical
340 direction, giving 2.56×10^6 , 99.2×10^3 , and 2.48×10^3 control volumes in total. The domain
341 contained two materials with contrasting hydraulic conductivities: Hanford and Ringold (Figure
342 4). Note that only the soil moisture and soil hydraulic properties within the top 3.8 m are
343 transferred from PFLOTRAN to CLM4.5 to allow simulations of infiltration, evaporation, and
344 transpiration in the next time step, as the CLM4.5 subsurface domain is limited to 3.8 meters and
345 cannot currently be easily modified. The hydrogeological properties of the Hanford and Ringold

346 materials (Table 2) were taken from *Williams et al.* [2008]. The unsaturated hydraulic
347 conductivity in PFLTORAN simulations was computed using the Van Genuchten water retention
348 function [*van Genuchten*, 1980] and the Burdine permeability relationship [*Burdine*, 1953].

349 We applied time varying pressure boundary conditions to PFLOTTRAN's subsurface domain
350 at the northern, western, and southern boundaries. The transient boundary conditions were
351 derived using kriging-based interpolations of hourly water table elevation measurements in wells
352 inside and beyond the model domain, following the approach used by *Chen et al.* [2013].
353 Transient head boundary conditions were applied at the eastern boundary with water table
354 elevations from the river gaging station and the gradient along the river estimated using water
355 elevations simulated by a 1-D hydraulic model along the reach, the Modular Aquatic Simulation
356 System in 1-Dimension (MASS1) [*Waichler et al.*, 2005], with a Nash–Sutcliffe coefficient
357 [*Nash and Sutcliffe*, 1970] of 0.99 in the simulation period (figure not shown). The river stage
358 simulated by MASS1 was also used to fill river stage measurement gaps caused by instrument
359 failures. A conductance value of 10^{-12} m was applied to the eastern shoreline boundary to mimic
360 the damping effect of low-permeability material on the river bed [*Hammond and Lichtner*,
361 2010]. A no-flow boundary condition was specified at the bottom of the domain to represent the
362 basalt underlying the Ringold formation.

363 Vegetation types (Figure 3b) were converted to corresponding CLM4.5 plant functional types
364 (PFTs) and bare soil (Figure 5). At each resolution, fractional area coverages of PFTs and bare
365 soil are determined based on the base map and written into the surface dataset as CLM4.5 inputs
366 (figures 5, S1, and S2). The CLM4.5 domain is terrain-following by treating the land surface as
367 the top of the subsurface domain, which is hydrologically active to a depth of 3.8 m. The
368 topography of the domain is retrieved from the 1-m topography and bathymetry dataset
369 [*Coleman et al.*, 2010] based on the North American Vertical Datum of 1988 (NAD88) and
370 resampled to each resolution (Figure S3).

371 The simulations were driven by hourly meteorological forcing from the Hanford
372 meteorological stations and hourly river stage from the gaging station over the period of 2009-
373 2015. Precipitation, wind speed, air temperature, and relative humidity were taken from the 300
374 Area meteorological station (longitude 119.726° , latitude 46.578°), located ~ 1.5 km from the
375 modeling domain. Other meteorological variables, such as downward shortwave and longwave

376 radiation, were obtained from the Hanford Meteorological station (longitude 119.599°, latitude
377 46.563°) located in the center of the Hanford site. The first two years of simulations (i.e., 2009
378 and 2010) were discarded as the spin-up period, so that 2011-2015 is treated as the simulation
379 period in the analyses.

380 Among the hydro-climatic forcing variables (e.g., river stage, surface air temperature,
381 incoming shortwave radiation, and total precipitation), river stage displayed the greatest inter-
382 annual variability (Figure 6). During the study period, high river stages occurred in early summer
383 of 2011 and 2012 due to the melt of above-average winter snow packs in the upstream drainage
384 basin, typical flow conditions occurred in 2013 and 2014, while 2015 was a year with low
385 upstream snow accumulation. Meanwhile, the meteorological variables, especially temperature
386 and shortwave radiation, do not show much inter-annual variability or trend, while precipitation
387 in late spring (i.e., May) of 2012 is higher than that in the other years, coincident with the high
388 river stage in 2012. In the “elevated” experiments (i.e., S_{E2m} , S_{E10m} , and S_{E20m}), the observed
389 river stage (meters based on NAD88) was increased by five meters at each hourly time step to
390 mimic a perturbed hydro-climatic condition in response to future warming.

391 To evaluate effects of river water and groundwater exchanges on land surface energy
392 partitioning, we separated the study domain for the 2-m simulations with lateral water exchange
393 (i.e., S_{2m} and S_{E2m}) into two sub-domains based on 2-m topography (shown in Figure S3a): (a)
394 the inland domain where the surface elevation is higher than 110 m; and (b) the riparian zone
395 where the surface elevation is less than or equal to 110 m. In addition to the latent heat flux, the
396 evaporative fraction, defined as the ratio of the latent heat flux to the sum of latent and sensible
397 heat fluxes was calculated over the sub-domains for both observed and elevated conditions at a
398 daily time step for all days with significant energy inputs (i.e., when net radiation is greater than
399 50 W m^2). The evaporative is an indicator of the type of surface as summarized in literature
400 [Lewis, 1995]: it is typically less than one over surfaces with abundant water supplies, ranges
401 between 0.75-0.9, 0.5-0.7, 0.15-0.3 for tropical rainforests, temperate forests and grasslands,
402 semi-arid landscapes, respectively, and approaches 0 over deserts.

403 To better quantify the spatio-temporal dynamics of stream-aquifer interactions, a
404 conservative tracer with a mole fraction of one was applied at the river boundary to track the flux
405 of river water and its total mass in the subsurface domain. While a constant concentration was

406 maintained at the river (i.e., eastern) boundary, the tracer was allowed to be transported out of
407 the northern, western, and southern boundaries. Water infiltrating at the upper boundary based on
408 CLM4.5 simulations was set to be tracer free, while a zero-flux tracer boundary condition was
409 applied at the lower boundary. The initial flow condition was a hydrostatic pressure distribution
410 based on the water table, as interpolated from the same set of wells that were used to create the
411 transient lateral flow boundary conditions at the northern, western, and southern boundaries. The
412 initial conservative tracer concentration was set to be zero for all mesh elements in the domain.
413 The simulations were started on 1 January 2009 and the first two years were discarded as the
414 spin-up period in the analysis. The mass of tracers in the domain and the fluxes of tracers across
415 the boundary allow us to quantitatively understand how river water is retained and transported in
416 the subsurface domain.

417 In addition to the CP v1.0 simulation, a standalone CLM4.5 simulation was also configured
418 and performed (i.e., CLM_{2m} in Table 1). CLM_{2m} shared the same subsurface properties and
419 initial conditions as the CLM4.5 setup in S_{2m} and S_{v2m} where CP v1.0 were used. However, we
420 note that CLM_{2m} simulations are not directly comparable to other simulations listed in Table 1
421 for the following reasons: (1) The CLM4.5 simulates subsurface hydrologic processes only up
422 down to 3.8 m below the surface, while in the CP v1.0 subsurface domain extends up to ~30 m
423 below the surface; (2) as discussed in section 2.1, CLM4.5 uses TOPMODEL-based
424 parameterizations to simulate surface and subsurface runoffs, as well as mean groundwater table
425 depth using formulations derived from catchment hydrology that are only applicable at coarser
426 resolutions; and (3) The key hydrologic processes (i.e., the exchange of river water and
427 groundwater at the east boundary and lateral transfer of water at all other boundaries) that affect
428 the hydrologic budget of the system are missing from CLM4.5. Therefore, the simulated latent
429 heat fluxes from CLM_{2m} are only the simulation was performed to provided as a reference for
430 interested readers to understand characterize how the physical parameterizations from one scale
431 (i.e., catchment scale) could affect the simulations when being used at another scale (i.e., field
432 scale) where those physical parameterizations do may not apply. in Figure S4 and were not
433 analyzed in section 4.

434

435 4 Results

436 4.1 Model evaluation

437 For the 3-D numerical experiments driven by the observed river stage time series (i.e., S_{2m} ,
438 S_{10m} , S_{20m}), CP v1.0 simulated soil water pressure was converted to water table depth and
439 compared against observed values at selected wells that were distributed throughout the domain
440 and of variable distances from the river (Figures 7, [S5-S4](#) and Table 3). The model performed
441 very well in simulating the temporal dynamics of the water table at all resolutions. The root-
442 mean-square errors were 0.028 m, 0.028 m, and 0.023 m at 2-m, 10-m, and 20-m resolutions,
443 respectively. The corresponding Nash–Sutcliffe coefficients were 0.998, 0.998, and 0.999. It was
444 surprising that the performance metrics at 20-m resolution matches the observations better than
445 those at finer resolutions, but the differences were marginal given the close match between the
446 model simulation results and observations. River stage was clearly the dominant driving factor
447 for water table fluctuations at the inland wells. In addition, errors in water and tracer budget
448 conservations, and surface energy conservation for each time step in S_{2m} are shown in figures
449 [S6a-S5a](#), b, and c respectively. The errors are sufficiently small when compared to the
450 magnitudes of the related fluxes to ensure faithful simulations in CP v1.0. These results indicated
451 that the coupled model was capable of simulating dynamic stream-aquifer interactions in the near
452 shore groundwater aquifer that experiences pressure changes induced by river stage variations at
453 sub-daily time scales.

454 4.2 Effect of stream-aquifer interactions on land surface energy partitioning

455 Next we evaluated the role of water table fluctuations on land surface variables, including
456 latent heat (LH) and sensible heat (SH) fluxes. The site is characterized by an approximate 10 m
457 vadose zone and surface fluxes and groundwater dynamics are typically decoupled [*Maxwell and*
458 *Kollet, 2008*], especially over the inland portion of the domain covered by shallow-rooted PFTs
459 and with higher surface elevations. However, river discharge and water table elevation displayed
460 large seasonal and inter-annual variability in the study period. Therefore, we selected the month
461 of June in each year to assess potential land surface-groundwater coupling because it is the
462 month of peak river stage, while energy input is high and relatively constant across the years
463 (Figure 8a).

464 In June 2011 and 2012, high river stages push the groundwater table to ~108 m (or ~6 m
465 below the land surface). Groundwater at that elevation can affect land surface water and energy
466 exchanges with the atmosphere. The shrubs, including the patch of Basin big sagebrush and the
467 mixture of rabbitbrush and bunchgrass on the slope close to the river, are able to tap into the
468 elevated water table with their deeper roots. In the inland portion of the domain, capillary supply
469 was most evident in high-water years (i.e., 2011 and 2012), remains influential in normal years
470 (i.e., 2013 and 2014), and is essentially disabled in low-water years (i.e., 2015). The lateral
471 discharge of shallow groundwater to the river led to a band of negative difference in LH between
472 S_{2m} and S_{v2m} at the river boundary when the stage was low due to a decrease in rooting zone soil
473 moisture for evapotranspiration by the riparian trees (Figure 8b). This pattern was most evident
474 in June 2015. Such a mechanism decreases in high-water and normal years because of more
475 frequent inundation of the river bank and groundwater gradient reversal.

476 Driven by elevated river stages, land surface energy partitioning in S_{E2m} (figures 9 and 10)
477 was significantly shifted from that in S_{2m} (Figure 8a) through two mechanisms: (1) expanding
478 the periodically inundated fraction of the riparian zone (i.e., surface elevation ≤ 110 m); and (2)
479 enhancing moisture availability in the vadose zone in the inland domain (i.e., surface elevation $>$
480 110 m) through capillary rise. Both mechanisms led to general increases in simulated vadose-
481 zone moisture availability and therefore higher latent heat fluxes compared to the simulations
482 driven by the observed condition. For the inland domain, evaporative fraction clearly displayed
483 an increasing trend as the groundwater table level becomes shallower, consistent between the
484 simulations (Figure 10c). The daily evaporative fractions for the inland domain stayed well
485 below 0.2 when the water table levels are less than 112 m, suggesting decoupled surface-
486 subsurface conditions in a typical semi-arid environment. When water table levels increased to
487 be above 112 m, the evaporative fraction increases to ~0.2, indicating that the surface and
488 subsurface processes become more strongly coupled because of improved water availability for
489 evapotranspiration, especially in the elevated simulation (i.e., S_{E2m}). Evaporative fraction in the
490 riparian zone remained close to 1.0, suggesting strong influences of the river and the role of
491 deeper rooted plant types (e.g., riparian trees and shrubs) in modulating the energy partitioning
492 (Figure 10d) of riparian zones in the semi-arid to arid environments.

493 To confirm the above findings, the liquid saturation [*unitless*] and mass of river water [*mol*]
494 in the domain from S_{2m} and S_{E2m} on 30 June each year are plotted along a transect perpendicular

495 | to the river ($y = 200$ m) in figures 11 and [S7S6](#), and across a x-y plane at an elevation of 107 m
496 | in figures [S8-S7](#) and [S9S8](#), respectively. Driven by the pressure introduced by elevated river
497 | stages, river water not only intruded further toward or even across the western boundary in high
498 | water years, but also led to shallower water table and increased liquid saturation in the vadose
499 | zone due to capillary rise across the domain. In fact, liquid saturation in the shallow vadose zone
500 | could increase from 0.1-0.2 in S_{2m} to 0.3-0.4 in S_{E2m} on these days because of river water
501 | intrusion. The river-water tracer could show up in the near-surface vadose zone at a distance of
502 | ~400 m from the river (Figure [S7S6](#)). Interestingly, by comparing the spatial distributions of
503 | river-water tracer in the low-water year (i.e., 2015) between the “observed” and “elevated”
504 | scenarios, the presence of river water in the domain was much less in the elevated scenario in
505 | terms of its spatial coverage (figures 11 and [S7S6](#)). This pattern suggests that after a number of
506 | years of enhanced river water intrusion into the domain, the hydraulic gradient between
507 | groundwater and river-water could be reversed, so that groundwater discharging might be
508 | expected more frequently in low-water years in a prolonged elevated scenario.

509 | The responses of LH and evaporative fraction (figures 9 and 10) indicated that a tight
510 | coupling among stream, aquifer, and land surface processes occurred in the elevated scenario,
511 | which could become realistic in one to two decades for the study site, or for other sites along the
512 | Hanford reach characterized by lower elevations under the current condition.

513 | As discussed in sections 2.1 and 3.2., the hydrologic parameterizations in the default CLM4.5
514 | model are based on conceptual and physical understandings from watershed hydrology that do
515 | not apply at the scale of our study site, where the exchange of river water and groundwater
516 | dominates the hydrologic budget of the system. Nevertheless, a comparison between CLM4.5
517 | and CP v1.0 helps characterize how scale inconsistencies in physical representations affect the
518 | simulations. Figure 12 shows comparisons of key components in the hydrologic budget between
519 | the two models. The simulated mean water table elevation of the domain from CLM4.5 ranges
520 | between 74 m and 80 m (i.e., 35 m – 40 m below the surface), while the observed water table
521 | elevation ranges between 104 m and 108 m (i.e., 5 m – -10 m below the surface), and was
522 | accurately reproduced by S_{2m} (Figure 12a). By using physics derived for the larger scale,
523 | CLM4.5 could not capture subsurface river water and groundwater exchanges, and consequently
524 | cannot accurately simulate groundwater table dynamics for our study domain.

525 At this semi-arid field site, the groundwater and -river water exchanges represented in S_{2m}
526 recharges the unconfined aquifer, and hence maintains sufficient soil water availability in the top
527 3.8 m of the soil column, while the lack of groundwater and river water interactions in CLM_{2m}
528 leads to overall declining soil water content with seasonal variability as a result of percolation of
529 winter rain water (Figure 12b). The difference in soil moisture availability propagates to
530 evapotranspiration (ET) and its components (figures 12c-f). Simulated summer ET in CLM_{2m}
531 shows a high-frequency signal in response to rainfall pulses through ground evaporation.
532 Transpiration simulated by CLM_{2m} is determined by soil water availability in the soil column. In
533 the spring and early summer of 2011 and 2013, transpiration from CLM_{2m} is close to that from
534 S_{2m} given sufficient soil water. For other periods, CLM_{2m} simulates significant lower
535 transpiration rates compared to S_{2m} .

536 Simulated latent heat fluxes in June for the period of 2011-2015 from CLM_{2m} and their
537 differences from those in S_{2m} are also illustrated in figures S9a and b. Evidently, the hydrologic
538 gradient from river to inland is missing as CLM4.5 lacks the capability of capturing the river
539 stage dynamics at such a resolution (in Figure S9a). Instead, even though initiated from the same
540 initial condition as S_{2m} on 01/01/2009 as discussed in the spin-up procedure in section 3.2, soil
541 moisture at the grid cells inundated or periodically inundated by the river is soon depleted
542 through ET, surface runoff, or baseflow. On the other hand, latent heat from the inland domain is
543 generally higher in CLM_{2m} than in S_{2m} due to ground evaporation in response to rainfall pulses.
544 In short, CLM4.5 fails to capture the dynamics of groundwater and river water exchanges. These
545 biases propagates to simulated water and energy fluxes, which could have large impacts on
546 boundary layer evolution, convection, and cloud formation in coupled land-atmosphere studies.

547 **4.3 Effect of spatial resolution**

548 To apply the model to large-scale simulations or over a long time period, it is important to assess
549 how the model performs at coarser resolution, as the 2-m simulations are computationally
550 expensive. Here, we use the 2-m simulations (i.e., S_{2m} and S_{E2m}) simulations as benchmarks for
551 this assessment. That is, S_{2m} and S_{E2m} simulated variables are treated as the “truth” for
552 “observed” and “elevated” river stage scenarios, and outputs from other simulations are
553 compared to them to verify their performance. In the previous section, we showed that simulated

554 water table levels from the model were virtually identical to observations. In this section, we
555 further quantify biases of other variables of interest from the high-fidelity 2-m simulations.

556 The domain-averaged daily surface energy fluxes from S_{2m} show clear seasonal patterns,
557 which are consistent in terms of their magnitudes and timing, reflecting mean climate conditions
558 at the site (Figure S10). Driven by elevated river stages, latent heat from S_{E2m} is consistently
559 higher than that from S_{2m} . The mean latent heat and sensible heat fluxes simulated by S_{2m} were
560 14.1 W m^{-2} and 38.7 W m^{-2} over this period, compared to by 18.50 W m^{-2} and 35.75 W m^{-2} in
561 S_{E2m} . Figure 42-13 shows deviations of simulated LH and SH in the 20-m and 10-m simulations
562 from the corresponding 2-m simulations. The deviations of both LH and SH were small across
563 all the simulations driven by the observed river stage when surface and subsurface were
564 decoupled. In the elevated simulations (i.e., S_{E10m} and S_{E20m}) when surface and subsurface
565 processes are more tightly coupled, errors in surface fluxes became significant in the coarse
566 resolution simulations when compared to S_{E2m} . For example, the relative errors in LH were
567 2.41% and 1.35% for S_{20m} and S_{10m} , respectively, as compared to S_{2m} , but grew as large as
568 33.84% and 33.19% for S_{E20m} and S_{E10m} , respectively, when compared to S_{E2m} . The 10-m
569 simulations outperformed the 20-m simulations under both scenarios but the magnitudes of
570 errors were comparable. On the other hand, notably the vertical only simulation (S_{v2m}) has a
571 small error of 5.67% in LH compared to S_{2m} , indicating that lateral flow is less important when
572 water table is deep.

573 To better understand how water in the river and the aquifer was connected, we also
574 quantified the biases of subsurface state variables and fluxes including total water mass and
575 tracer amount, as well as exchange rates of water and tracer at four boundaries of the subsurface
576 domain using a similar approach (Figure S11 and Figure 4314). Compared to the magnitude of
577 total water mass in the domain (averaged $919.45 \times 10^6 \text{ Kg}$ and $1020.19 \times 10^6 \text{ Kg}$ in S_{2m} and
578 S_{E2m}), errors introduced by coarsening the resolution were very small under the observed river
579 stage condition (0.04% for S_{20m} and 0.03% for S_{10m}) and grew to 9.85% for S_{E20m} and 9.87% for
580 S_{E10m} in terms of total water mass in the domain (Table 5). However, for total tracer in the
581 domain (averaged $142.07 \times 10^6 \text{ mol}$ and $172.46 \times 10^6 \text{ mol}$ in S_{2m} and S_{E2m}) as a result of transport
582 of river water in lateral and normal directions to the river, resolution clearly makes a difference
583 under both observed condition and elevated scenarios (relative errors of 5.44% for S_{10m} , 10.40%
584 for S_{20m} , and 22.0% for both S_{E10m} and S_{E20m}). The magnitude of computed mass exchange rates

585 at the four boundaries (Figure S11) indicates that a coarse resolution promotes larger river water
586 fluxes and groundwater exchanges, especially during the period of spring river stage increase
587 under the elevated scenario. This forcing contributes to a significant bias in total tracer amount
588 by the end of the simulation. The exchange rates at the other three boundaries follow the same
589 pattern but with smaller magnitudes, especially for the west boundary that requires a significant
590 gradient high enough to push river water further inland.

591 The results of simulations at three different resolutions indicated that: (1) the partitioning of
592 the land surface energy budget is mainly controlled by near-surface moisture. Spatial resolution
593 did not seem to be a significant factor in the computation of surface energy fluxes when the
594 water table was deep at the semi-arid site; (2) if the surface and subsurface are tightly coupled as
595 in the elevated river stage simulations, resolution becomes an important factor to consider for
596 credible simulations of the surface fluxes, as the land surface, subsurface, and riverine processes
597 are expected to be more connected and coupled; (3) regardless of whether a tight coupling
598 between the surface and subsurface occurs, if mass exchange rates and associated
599 biogeochemical reactions in the aquifer are of interest, a higher resolution is desired close to the
600 river shoreline to minimize terrain errors.

601

602 **5 Discussion and future work**

603 A coupled three-dimensional surface and subsurface land model was developed and applied to a
604 site along the Columbia River to simulate interactions among river water, groundwater, and land
605 surface processes. The model features the coupling of the open-source and state-of-the-art
606 models portable on HPCs, the multi-physics reactive transport model PFLOTRAN and the
607 CLM4.5. Both models are under active development and testing by their respective communities,
608 therefore the coupled model could be updated to newer versions of PFLOTRAN and/or CLM to
609 facilitate transfer of knowledge in a seamless fashion. The coupled model represents a new
610 addition to the integrated surface and subsurface suite of models.

611 By applying the coupled model to a field site along the Columbia River shoreline driven by
612 highly dynamic river boundary conditions resulting from upstream dam operations, we
613 demonstrated that the model can be used to advance mechanistic understanding of stream-
614 aquifer-land interactions surrounding near-shore alluvial aquifers that experience pressure

615 changes induced by river stage variations along managed river reaches, which are of global
616 significance as a result of over 30,000 dams constructed worldwide during the past half century.
617 The land surface, subsurface, and riverine processes along such managed river corridors are
618 expected to be more strongly coupled under projected hydro-climatic regimes as a result of
619 increases in winter precipitation and early snowmelt. The dataset presented in this study can
620 serve as a good benchmarking case for testing other coupled models for their applications to such
621 systems. More data needs to be collected to facilitate the application and validation of the model
622 to a larger domain for understanding the contribution of near-shore hydrologic exchange to water
623 retention, biogeochemical cycling, and ecosystem functions along the river corridors.

624 [By comparing simulations from the coupled model \(CPv1.0\) to that from CLM4.5, we](#)
625 [demonstrated that the catchment-scale physics imbedded in CLM4.5 does not apply at the field](#)
626 [scale. By misrepresenting, or not including, key hydrologic processes at the scale of interest,](#)
627 [CLM4.5 fails to capture groundwater table dynamics, which could propagate to water and energy](#)
628 [budgets and have profound impacts on boundary layer, convection, and cloud formation in](#)
629 [coupled land-atmosphere studies. Our finding is consistent with results from other recent studies](#)
630 [in which integrated surface and subsurface models were compared to standalone land surface](#)
631 [models \[Fang et al., 2017; Niu et al., 2017\].](#)

632 By benchmarking the coarser resolution simulations at 20 m and 10 m against the 2-m
633 simulations, we find that resolution is not a significant factor for surface flux simulations when
634 the water table is deep. However, resolution becomes important when the surface and subsurface
635 processes are tightly coupled, and for accurately estimating the rate of mass exchange at the
636 riverine boundaries, which can affect the calculation of biogeochemical processes involved in
637 carbon and nitrogen cycles.

638 Our numerical experiments suggested that riverine, land surface, and subsurface processes
639 could become more tightly coupled through two mechanisms in the near-shore environments: (1)
640 expanding the periodically inundated fraction of the riparian zone and (2) enhancing moisture
641 availability in the vadose zone in the inland domain through capillary rise. Both mechanisms can
642 lead to increases in vadose-zone moisture availability and higher evapotranspiration rates. The
643 latter is critical for understanding ecosystem functioning, biogeochemical cycling, and land-
644 atmosphere interactions along river corridors in arid and semi-arid regions that are expected to

645 experience new hydro-climatic regimes in a changing climate. However, these systems have
646 been poorly accounted for in current-generation Earth system models and therefore require more
647 attention in future studies.

648 We acknowledge that there are a number of limitations of this study that need to be addressed
649 in future studies:

650 (1) Motivated by understanding the stream-aquifer-land interactions with a focus on
651 groundwater and river water interactions along a river corridor situated in a semi-arid climate,
652 the river boundary conditions were prescribed using observations with gaps filled by a 1-D
653 hydrodynamics model. Future versions of the CP model need to incorporate two-way
654 interactions between stream and aquifer by developing a surface flow component and testing the
655 new implementation against standard benchmark cases [Kollet *et al.*, 2017; Maxwell *et al.*,
656 2014].

657 (2) We note that CLM estimates the surface heat and moisture fluxes using the Monin-
658 Obukhov Similarity Theory (section 2.1), which is only valid when the surface layer depth $z \gg z_0$,
659 where z_0 is the aerodynamic roughness length. As reviewed by Basu and Lacser [2017], it is
660 highly recommended that $z > 50z_0$, which should be proportional to the horizontal grid spacing
661 to guarantee the validity of the Monin-Obukhov Similarity Theory [Arnqvist and Bergström,
662 2015]. In our simulations, the majority of the Hanford 300A domain is covered by bare soil ($z_0 =$
663 0.01 m), grass ($z_0 = 0.013$ m), shrubs ($z_0 = 0.026-0.043$ m), and riparian trees (varies across the
664 seasons, $z_0 = 0.008$ m when LAI = 2 in the summer and $z_0 = 1.4$ when LAI = 0 in the winter).
665 Therefore, a 2-m resolution is sufficiently coarse under most conditions except for the grid cells
666 covered by riparian trees in the winter. Nevertheless, the wintertime latent heat and sensible heat
667 fluxes are nearly zero due to extremely low energy inputs. Therefore, the 2-m simulations
668 supported by the dense groundwater monitoring network at the site provide a valid benchmark
669 for the coarser resolution simulations. For future applications of the coupled model, caution
670 should be taken to evaluate the site condition for the validity of model parameterizations.

671 (3) We used the simulated surface energy fluxes from S_{2m} to verify coarser-resolution
672 simulations. The simulated surface energy flux needs to be validated against eddy covariance
673 tower observations, which are not available yet at the site. Nevertheless, we have made initial
674 efforts to install eddy covariance systems at the site (see description in section 3.1 of Gao *et al.*

675 [2017]) but the processing the flux data is still preliminary. We will report flux observations and
676 validations of the surface energy budget simulations in future studies.

677 (4) Even when observed fluxes are available for validation, the model structural problems
678 associated with ET parameterizations in CLM4.5 need to be addressed for reasonable
679 simulations of the ET components, especially for the study site. That is, it has been well-
680 documented that ET simulated by CLM4.5 and CLM4 could be enhanced when vegetation is
681 removed. This ET enhancement over bare soil has been documented as a counter-intuitive bias
682 for most unsaturated soils in CLM4 and CLM4.5 simulations [Lawrence *et al.*, 2012; Tang and
683 Riley, 2013a]. Tang and Riley [2013a] explored a few potential causes for this likely bias (e.g.,
684 soil resistance, litter layer resistance, and numerical time step). They found the implementation
685 of a physically based soil resistance lowered the bias slightly, but concluded that the bias
686 remained [Tang and Riley, 2013b]. Meanwhile, in studying ET over semiarid regions, Swenson
687 and Lawrence [2014] proposed another soil resistance formulation to fix this excessive soil
688 evaporation problem within CLM4.5. While their modification improved the simulated terrestrial
689 water storage anomaly and ET when compared to GRACE data and FLUXNET-MTE data,
690 respectively, the empirical nature of the soil resistance proposed could have underestimated the
691 soil resistance variability when compared to other estimates [Tang and Riley, 2013b].
692

693 **Code availability**

694 CLM4.5 is an open-source software released as part of the Community Earth System Model
695 (CESM) version 1.2 (<http://www.cesm.ucar.edu/models/cesm1.2>). The version of CLM4.5 used
696 in CP v1.0 is a branch from the CLM developer's repository. Its functionality is scientifically
697 consistent with descriptions in *Oleson et al.* [2013] with source codes refactored for a modular
698 code design. Additional minor code modifications were added by the authors to support coupling
699 with PFLOTRAN. Permission from the CESM Land Model Working Group has been obtained
700 to release this CLM4.5 development branch but the National Center for Atmospheric Research
701 cannot provide technical support for this version of the code CP v1.0. PFLOTRAN is an open-
702 source software distributed under the terms of the GNU Lesser General Public License as
703 published by the Free Software Foundation either version 2.1 of the License, or any later version.
704 The CP v1.0 has two separate, open-source repositories for CLM4.5 and PFLOTRAN at:

- 705 • https://bitbucket.org/clm_pflotran/clm-pflotran-trunk
- 706 • https://bitbucket.org/clm_pflotran/pflotran-clm-trunk

707 The README guide for the CP v1.0 and dataset used in this study are available from the open-
708 source repository https://bitbucket.org/pnnl_sbr_sfa/notes-for-gmd-2017-35.

709

710 **Acknowledgement**

711 This research was supported by the U.S. Department of Energy (DOE), Office of Biological and
712 Environmental Research (BER), as part of BER's Subsurface Biogeochemical Research Program
713 (SBR). This contribution originates from the SBR Scientific Focus Area (SFA) at the Pacific
714 Northwest National Laboratory (PNNL), [operated by Battelle Memorial Institute for the U.S.](#)
715 [DOE under contract DE-AC05-76RLO1830. We greatly appreciate the constructive comments](#)
716 [from two anonymous reviewers and the topical editor, Dr., Jatin Kala, which helped improve the](#)
717 [manuscript significantly.](#)

718

719 **References**

- 720 Arnqvist, J., and Bergström, H. (2015), Flux-profile relation with roughness sublayer correction,
721 *Quarterly Journal of the Royal Meteorological Society*, 141, 1191-1197, 10.1002/qj.2426, 2015.
- 722 Balay, S., J. Brown, K. Buschelman, V. Eijkhout, W. D. Gropp, D. Kaushik, M. G. Knepley, L.
723 C. McInnes, B. F. Smith, and H. Zhang (2015), PETSc Users Manual, Tech. Rep. ANL-95/11—
724 Revision 3.5*Rep.*, Argonne, Ill.
- 725 Basu, S., and Lacser, A. (2017). A Cautionary Note on the Use of Monin–Obukhov Similarity
726 Theory in Very High-Resolution Large-Eddy Simulations, *Boundary-Layer Meteorology*, 163,
727 351-355, 10.1007/s10546-016-0225-y.
- 728 Beven, K. J., and M. J. Kirkby (1979), A physically based, variable contributing area model of
729 basin hydrology / Un modèle à base physique de zone d'appel variable de l'hydrologie du bassin
730 versant, *Hydrological Sciences Bulletin*, 24(1), 43-69, doi:10.1080/02626667909491834.
- 731 Bjornstad, B. N. (2007), *On the Trail of the Ice Age Floods: A Geological Field Guide to the*
732 *Mid-Columbian Basin*, KeoKee, Sandpoint, ID.
- 733 Burdine, N. T. (1953), Relative Permeability Calculations From Pore Size Distribution Data,
734 doi:10.2118/225-G.
- 735 Chen, X., G. E. Hammond, C. J. Murray, M. L. Rockhold, V. R. Vermeul, and J. M. Zachara
736 (2013), Application of ensemble-based data assimilation techniques for aquifer characterization
737 using tracer data at Hanford 300 area, *Water Resources Research*, 49(10), 7064-7076,
738 doi:10.1002/2012WR013285.
- 739 Chen, X., H. Murakami, M. S. Hahn, G. E. Hammond, M. L. Rockhold, J. M. Zachara, and Y.
740 Rubin (2012), Three-dimensional Bayesian geostatistical aquifer characterization at the Hanford
741 300 Area using tracer test data, *Water Resources Research*, 48(6), n/a-n/a,
742 doi:10.1029/2011WR010675.
- 743 Clark, M. P., et al. (2015), Improving the representation of hydrologic processes in Earth System
744 Models, *Water Resources Research*, 51(8), 5929-5956, doi:10.1002/2015WR017096.
- 745 Coleman, A., K. Larson, D. Ward, and J. Lettrick (2010), Development of a High-Resolution
746 Bathymetry Dataset for the Columbia River through the Hanford Reach*Rep. PNNL-19878*,
747 Pacific Northwest National Laboratory, Richland, WA.
- 748 Condon, L. E., R. M. Maxwell, and S. Gangopadhyay (2013), The impact of subsurface
749 conceptualization on land energy fluxes, *Advances in Water Resources*, 60(0), 188-203,
750 doi:http://dx.doi.org/10.1016/j.advwatres.2013.08.001.
- 751 Craig, A. P., M. Vertenstein, and R. Jacob (2012), A new flexible coupler for earth system
752 modeling developed for CCSM4 and CESM1, *International Journal of High Performance*
753 *Computing Applications*, 26(1), 31-42, doi:10.1177/1094342011428141.
- 754 Elsner, M. M., L. Cuo, N. Voisin, J. S. Deems, A. F. Hamlet, J. A. Vano, K. E. B. Mickelson, S.
755 Y. Lee, and D. P. Lettenmaier (2010), Implications of 21st century climate change for the
756 hydrology of Washington State, *Climatic Change*, 102(1-2), 225-260, doi:DOI 10.1007/s10584-
757 010-9855-0.

758 Fan, Y., H. Li, and G. Miguez-Macho (2013), Global Patterns of Groundwater Table Depth,
759 *Science*, 339(6122), 940-943.

760 Fan, Y., and G. Miguez-Macho (2011), A simple hydrologic framework for simulating wetlands
761 in climate and earth system models, *Climate Dynamics*, 37(1), 253-278, doi:10.1007/s00382-
762 010-0829-8.

763 [Fang, Y., L. R. Leung, Z. Duan, M. S. Wigmosta, R. M. Maxwell, J. Q. Chambers, and J.
764 Tomasella \(2017\), Influence of landscape heterogeneity on water available to tropical forests in
765 an Amazonian catchment and implications for modeling drought response, *J. Geophys. Res.*
766 *Atmos.*, 122, 8410–8426, doi:10.1002/2017JD027066.](#)

767 Fischer, H., F. Kloeppel, S. Wilzcek, and M. T. Pusch (2005), A river's liver - microbial processes
768 within the hyporheic zone of a large lowland river, *Biogeochemistry*, 76(2), 349-371.

769 Gaillardet, J., P. Regnier, R. Lauerwald, and P. Ciais (2014), Geochemistry of the Earth's surface
770 GES-10 Paris France, 18-23 August, 2014. Carbon Leakage through the Terrestrial-
771 aquatic Interface: Implications for the Anthropogenic CO₂ Budget, *Procedia Earth and
772 Planetary Science*, 10, 319-324, doi:http://dx.doi.org/10.1016/j.proeps.2014.08.025.

773 Gao, Z., Russell, E. S., Missik, J. E. C., Huang, M., Chen, X., Strickland, C. E., Clayton, R.,
774 Arntzen, E., Ma, Y., and Liu, H. (2017). A novel approach to evaluate soil heat flux calculation:
775 An analytical review of nine methods, *Journal of Geophysical Research: Atmospheres*, n/a-n/a,
776 10.1002/2017JD027160.

777 Gebler, S., Hendricks Franssen, H. J., Kollet, S. J., Qu, W., and Vereecken, H.: High resolution
778 modelling of soil moisture patterns with TerrSysMP: A comparison with sensor network data,
779 *Journal of Hydrology*, 547, 309-331, <https://doi.org/10.1016/j.jhydrol.2017.01.048>, 2017.

780 Gilbert, J. M., Maxwell, R. M., and Gochis, D. J.: Effects of Water-Table Configuration on the
781 Planetary Boundary Layer over the San Joaquin River Watershed, California, *Journal of
782 Hydrometeorology*, 18, 1471-1488, 10.1175/jhm-d-16-0134.1, 2017.

783 Hamlet, A. F., and D. P. Lettenmaier (1999), Effects of climate change on hydrology and water
784 resources in the Columbia River basin, *Journal of the American Water Resources Association*,
785 35(6), 1597-1623.

786 Hammond, G. E., and P. C. Lichtner (2010), Field-scale model for the natural attenuation of
787 uranium at the Hanford 300 Area using high-performance computing, *Water Resources
788 Research*, 46(9), n/a-n/a, doi:10.1029/2009WR008819.

789 Hammond, G. E., P. C. Lichtner, and R. T. Mills (2014), Evaluating the performance of parallel
790 subsurface simulators: An illustrative example with PFLOTRAN, *Water Resources Research*,
791 50(1), 208-228, doi:10.1002/2012WR013483.

792 Hammond, G. E., P. C. Lichtner, and M. L. Rockhold (2011), Stochastic simulation of uranium
793 migration at the Hanford 300 Area, *Journal of Contaminant Hydrology*, 120-21, 115-128,
794 doi:DOI 10.1016/j.jconhyd.2010.04.005.

795 Harvey, J., and M. Gooseff (2015), River corridor science: Hydrologic exchange and ecological
796 consequences from bedforms to basins, *Water Resources Research*, 51(9), 6893-6922,
797 doi:10.1002/2015WR017617.

798 Hauer, C., Siviglia, A., and Zolezzi, G.: Hydropeaking in regulated rivers – From process
799 understanding to design of mitigation measures, *Science of The Total Environment*, 579, 22-26,
800 <https://doi.org/10.1016/j.scitotenv.2016.11.028>, 2017.

801 Hou, Z., M. Huang, L. R. Leung, G. Lin, and D. M. Ricciuto (2012), Sensitivity of surface flux
802 simulations to hydrologic parameters based on an uncertainty quantification framework applied
803 to the Community Land Model, *Journal of Geophysical Research: Atmospheres (1984–2012)*,
804 117(D15).

805 Hurrell, J. W., et al. (2013), The Community Earth System Model: A Framework for
806 Collaborative Research, *Bulletin of the American Meteorological Society*, 94(9), 1339-1360,
807 doi:10.1175/bams-d-12-00121.1.

808 Ji, X., C. Shen, and W. J. Riley (2015), Temporal evolution of soil moisture statistical fractal and
809 controls by soil texture and regional groundwater flow, *Advances in Water Resources*, 86, Part
810 A, 155-169, doi:<http://dx.doi.org/10.1016/j.advwatres.2015.09.027>.

811 Karra, S., Painter, S. L., and Lichtner, P. C. (2014). Three-phase numerical model for subsurface
812 hydrology in permafrost-affected regions (PFLOTRAN-ICE v1.0), *The Cryosphere*, 8, 1935-
813 1950, 10.5194/tc-8-1935-2014, 2014.

814 Keune, J., Gasper, F., Goergen, K., Hense, A., Shrestha, P., Sulis, M., and Kollet, S. (2016),
815 Studying the influence of groundwater representations on land surface-atmosphere feedbacks
816 during the European heat wave in 2003, *Journal of Geophysical Research: Atmospheres*, 121,
817 13,301-313,325, 10.1002/2016JD025426, 2016.

818 Kollet, S. J., and R. M. Maxwell (2008), Capturing the influence of groundwater dynamics on
819 land surface processes using an integrated, distributed watershed model, *Water Resources*
820 *Research*, 44(2), n/a-n/a, doi:10.1029/2007WR006004.

821 Kollet, S., Sulis, M., Maxwell, R. M., Paniconi, C., Putti, M., Bertoldi, G., Coon, E. T., Cordano,
822 E., Endrizzi, S., Kikinzon, E., Mouche, E., Mügler, C., Park, Y.-J., Refsgaard, J. C., Stisen, S.,
823 and Sudicky, E. (2017).: The integrated hydrologic model intercomparison project, IH-MIP2: A
824 second set of benchmark results to diagnose integrated hydrology and feedbacks, *Water*
825 *Resources Research*, 53, 867-890, 10.1002/2016WR019191. Kumar, J., N. Collier, G. Bisht, R.
826 T. Mills, P. E. Thornton, C. M. Iversen, and V. Romanovsky (2016), Modeling the
827 spatiotemporal variability in subsurface thermal regimes across a low-relief polygonal tundra
828 landscape, *The Cryosphere*, 10(5), 2241-2274, doi:10.5194/tc-10-2241-2016.

829 Lawrence, P. J., Feddema, J. J., Bonan, G. B., Meehl, G. A., O'Neill, B. C., Oleson, K. W.,
830 Levis, S., Lawrence, D. M., Kluzek, E., Lindsay, K., and Thornton, P. E. (2012). Simulating the
831 Biogeochemical and Biogeophysical Impacts of Transient Land Cover Change and Wood
832 Harvest in the Community Climate System Model (CCSM4) from 1850 to 2100, *Journal of*
833 *Climate*, 25, 3071-3095, 10.1175/jcli-d-11-00256.1. Lei, H., M. Huang, L. R. Leung, D. Yang, X.
834 Shi, J. Mao, D. J. Hayes, C. R. Schwalm, Y. Wei, and S. Liu (2014), Sensitivity of global
835 terrestrial gross primary production to hydrologic states simulated by the Community Land
836 Model using two runoff parameterizations, *Journal of Advances in Modeling Earth Systems*,
837 6(3), 658-679.

838 Leng, G., M. Huang, N. Voisin, X. Zhang, G. R. Asrar, and L. R. Leung (2016a), Emergence of
839 new hydrologic regimes of surface water resources in the conterminous United States under
840 future warming, *Environmental Research Letters*, 11(11), 114003.

841 Leng, G., X. Zhang, M. Huang, Q. Yang, R. Rafique, G. R. Asrar, and L. R. Leung (2016b),
842 Simulating county-level crop yields in the conterminous United States using the community land
843 model: The effects of optimizing irrigation and fertilization, *Journal of Advances in Modeling*
844 *Earth Systems*, n/a-n/a, doi:10.1002/2016MS000645.

845 Leung, L. R., M. Huang, Y. Qian, and X. Liang (2011), Climate–soil–vegetation control on
846 groundwater table dynamics and its feedbacks in a climate model, *Climate Dynamics*, 36(1), 57-
847 81.

848 Lewis, J. M. (1995), The Story behind the Bowen Ratio, *Bulletin of the American*
849 *Meteorological Society*, 76(12), 2433-2443, doi:10.1175/1520-
850 0477(1995)076<2433:tsbtbr>2.0.co;2.

851 Liang, X., D. P. Lettenmaier, E. F. Wood, and S. J. Burges (1994), A simple hydrologically
852 based model of land surface water and energy fluxes for general circulation models, *Journal of*
853 *Geophysical Research: Atmospheres*, 99(D7), 14415-14428, doi:10.1029/94JD00483.

854 Lichtner, P. C., and G. E. Hammond (2012), Using High Performance Computing to Understand
855 Roles of Labile and Nonlabile Uranium(VI) on Hanford 300 Area Plume Longevity, *Vadose*
856 *Zone Journal*, 11(2), doi:10.2136/vzj2011.0097.

857 Lichtner, P. C., G. E. Hammond, C. Lu, S. Karra, G. Bisht, B. Andre, R. T. Mills, and K. Jitu
858 (2015), PFLOTRAN User Manual: a Massively Parallel Reactive Flow and Transport Model for
859 Describing Surface and Subsurface Processes *Rep.*

860 Liu, Y., G. Bisht, Z. M. Subin, W. J. Riley, and G. S. H. Pau (2016), A Hybrid Reduced-Order
861 Model of Fine-Resolution Hydrologic Simulations at a Polygonal Tundra Site, *Vadose Zone*
862 *Journal*, 15(2).

863 Maxwell, R. M., and L. E. Condon (2016), Connections between groundwater flow and
864 transpiration partitioning, *Science*, 353(6297), 377-380, doi:10.1126/science.aaf7891.

865 Maxwell, R. M., L. E. Condon, and S. J. Kollet (2015), A high-resolution simulation of
866 groundwater and surface water over most of the continental US with the integrated hydrologic
867 model ParFlow v3, *Geosci. Model Dev.*, 8(3), 923-937, doi:10.5194/gmd-8-923-2015.

868 Maxwell, R. M., and S. J. Kollet (2008), Interdependence of groundwater dynamics and land-
869 energy feedbacks under climate change, *Nature Geosci.*, 1(10), 665-669.

870 Maxwell, R. M., and N. L. Miller (2005), Development of a Coupled Land Surface and
871 Groundwater Model, *Journal of Hydrometeorology*, 6(3), 233-247, doi:10.1175/JHM422.1.

872 Maxwell, R. M., et al. (2014), Surface-subsurface model intercomparison: A first set of
873 benchmark results to diagnose integrated hydrology and feedbacks, *Water Resources Research*,
874 50(2), 1531-1549, doi:10.1002/2013WR013725.

875 McNamara, J. P., D. Chandler, M. Seyfried, and S. Achet (2005), Soil moisture states, lateral
876 flow, and streamflow generation in a semi-arid, snowmelt-driven catchment, *Hydrological*
877 *Processes*, 19(20), 4023-4038, doi:10.1002/hyp.5869.

878 Miguez-Macho, G., and Y. Fan (2012), The role of groundwater in the Amazon water cycle: 1.
879 Influence on seasonal streamflow, flooding and wetlands, *Journal of Geophysical Research:*
880 *Atmospheres*, 117(D15), n/a-n/a, doi:10.1029/2012JD017539.

881 Nash, J. E., and J. V. Sutcliffe (1970), River flow forecasting through conceptual models part I
882 — A discussion of principles, *Journal of Hydrology*, 10(3), 282-290,
883 doi:[http://dx.doi.org/10.1016/0022-1694\(70\)90255-6](http://dx.doi.org/10.1016/0022-1694(70)90255-6).

884 Nir, Y. K., L. Haibin, and F. Ying (2014), Groundwater flow across spatial scales: importance
885 for climate modeling, *Environmental Research Letters*, 9(3), 034003.

886 Niu, G.-Y., C. Paniconi, P. A. Troch, R. L. Scott, M. Durcik, X. Zeng, T. Huxman, and D. C.
887 Goodrich (2014), An integrated modelling framework of catchment-scale ecohydrological
888 processes: 1. Model description and tests over an energy-limited watershed, *Ecohydrology*, 7(2),
889 427-439, doi:10.1002/eco.1362.

890 Niu, G.-Y., Z.-L. Yang, R. E. Dickinson, and L. E. Gulden (2005), A simple TOPMODEL-based
891 runoff parameterization (SIMTOP) for use in global climate models, *Journal of Geophysical*
892 *Research: Atmospheres*, 110(D21), n/a-n/a, doi:10.1029/2005JD006111.

893 Niu, G.-Y., Z.-L. Yang, R. E. Dickinson, L. E. Gulden, and H. Su (2007), Development of a
894 simple groundwater model for use in climate models and evaluation with Gravity Recovery and
895 Climate Experiment data, *Journal of Geophysical Research: Atmospheres*, 112(D7), n/a-n/a,
896 doi:10.1029/2006JD007522.

897 [Niu, J., C. Shen, J.Q. Chambers, J.M. Melack, and W.J. Riley, 2017: Interannual Variation in
898 Hydrologic Budgets in an Amazonian Watershed with a Coupled Subsurface–Land Surface
899 Process Model. *J. Hydrometeor.*, 18, 2597–2617, <https://doi.org/10.1175/JHM-D-17-0108.1>](#)

900 Oleson, K. W., et al. (2013), Technical Description of version 4.5 of the Community Land Model
901 (CLM)Rep. Ncar Technical Note NCAR/TN-503+STR, National Center for Atmospheric
902 Research, Boulder, CO.

903 Pau, G. S. H., G. Bisht, and W. J. Riley (2014), A reduced-order modeling approach to represent
904 subgrid-scale hydrological dynamics for land-surface simulations: application in a polygonal
905 tundra landscape, *Geosci. Model Dev.*, 7(5), 2091-2105, doi:10.5194/gmd-7-2091-2014.

906 Pau, G. S. H., C. Shen, W. J. Riley, and Y. Liu (2016), Accurate and efficient prediction of fine-
907 resolution hydrologic and carbon dynamic simulations from coarse-resolution models, *Water*
908 *Resources Research*, 52(2), 791-812, doi:10.1002/2015WR017782.

909 Rahman, M., M. Sulis, and S. J. Kollet (2015), The subsurface-land surface-atmosphere
910 connection under convective conditions, *Advances in Water Resources*, 83, 240-249,
911 doi:10.1016/j.advwatres.2015.06.003.

912 Rihani, J. F., F. K. Chow, and R. M. Maxwell (2015), Isolating effects of terrain and soil
913 moisture heterogeneity on the atmospheric boundary layer: Idealized simulations to diagnose
914 land-atmosphere feedbacks, *Journal of Advances in Modeling Earth Systems*, 7(2), 915-937,
915 doi:10.1002/2014MS000371.

916 Riley, W. J., and C. Shen (2014), Characterizing coarse-resolution watershed soil moisture
917 heterogeneity using fine-scale simulations, *Hydrol. Earth Syst. Sci.*, 18(7), 2463-2483,
918 doi:10.5194/hess-18-2463-2014.

919 Sakaguchi, K., and Zeng, X.: Effects of soil wetness, plant litter, and under-canopy atmospheric
920 stability on ground evaporation in the Community Land Model (CLM3.5), *Journal of*
921 *Geophysical Research: Atmospheres*, 114, n/a-n/a, 10.1029/2008JD010834, 2009.

922 Schaller, M. F., and Y. Fan (2009), River basins as groundwater exporters and importers:
923 Implications for water cycle and climate modeling, *Journal of Geophysical Research:*
924 *Atmospheres*, 114(D4), n/a-n/a, doi:10.1029/2008JD010636.

925 Shen, C., J. Niu, and M. S. Phanikumar (2013), Evaluating controls on coupled hydrologic and
926 vegetation dynamics in a humid continental climate watershed using a subsurface-land surface
927 processes model, *Water Resources Research*, 49(5), 2552-2572, doi:10.1002/wrcr.20189.

928 Shen, C., W. J. Riley, K. M. Smithgall, J. M. Melack, and K. Fang (2016), The fan of influence
929 of streams and channel feedbacks to simulated water and carbon fluxes, *Water Resources*
930 *Research*, doi:10.1002/2015WR018086.

931 Shi, Y., K. J. Davis, C. J. Duffy, and X. Yu (2013), Development of a Coupled Land Surface
932 Hydrologic Model and Evaluation at a Critical Zone Observatory, *Journal of Hydrometeorology*,
933 14(5), 1401-1420, doi:10.1175/JHM-D-12-0145.1.

934 Shrestha, P., Sulis, M., Masbou, M., Kollet, S., and Simmer, C.: A Scale-Consistent Terrestrial
935 Systems Modeling Platform Based on COSMO, CLM, and ParFlow, *Monthly Weather Review*,
936 142, 3466-3483, 10.1175/mwr-d-14-00029.1, 2014.

937 Sulis, M., Williams, J. L., Shrestha, P., Diederich, M., Simmer, C., Kollet, S. J., and Maxwell, R.
938 M.: Coupling Groundwater, Vegetation, and Atmospheric Processes: A Comparison of Two
939 Integrated Models, *Journal of Hydrometeorology*, 18, 1489-1511, 10.1175/jhm-d-16-0159.1,
940 2017.

941 Swenson, S. C., and Lawrence, D. M.: Assessing a dry surface layer-based soil resistance
942 parameterization for the Community Land Model using GRACE and FLUXNET-MTE data,
943 *Journal of Geophysical Research: Atmospheres*, 119, 10,299-210,312, 10.1002/2014JD022314,
944 2014.

945 Tang, G., Yuan, F., Bisht, G., Hammond, G. E., Lichtner, P. C., Kumar, J., Mills, R. T., Xu, X.,
946 Andre, B., Hoffman, F. M., Painter, S. L., and Thornton, P. E.: Addressing numerical challenges
947 in introducing a reactive transport code into a land surface model: a biogeochemical modeling
948 proof-of-concept with CLM-PFLOTRAN 1.0, *Geosci. Model Dev.*, 9, 927-946, 10.5194/gmd-9-
949 927-2016, 2016.

950 Tang, J., and Riley, W. J. (2013a) Impacts of a new bare-soil evaporation formulation on site,
951 regional, and global surface energy and water budgets in CLM4, *Journal of Advances in*
952 *Modeling Earth Systems*, 5, 558-571, 10.1002/jame.20034, 2013a.

953 Tang, J. Y., and Riley, W. J. (2013b) A new top boundary condition for modeling surface
954 diffusive exchange of a generic volatile tracer: theoretical analysis and application to soil
955 evaporation, *Hydrol. Earth Syst. Sci.*, 17, 873-893, 10.5194/hess-17-873-2013, 2013b.

956 Taylor, R. G., et al. (2013), Ground water and climate change, *Nature Clim. Change*, 3(4), 322-
957 329.

958 Thorne, P. D., M. P. Bergeron, M. D. Williams, and V. L. Freedman (2006), Groundwater Data
959 Package for Hanford Assessments *Rep. PNNL-14753*, Pacific Northwest National Laboratory,
960 Richland, WA.

961 Tiffan, K. F., R. D. Garland, and D. W. Rondorf (2002), Quantifying flow-dependent changes in
962 subyearling fall chinook salmon rearing habitat using two-dimensional spatially explicit

963 modeling, *North American Journal of Fisheries Management*, 22(3), 713-726, doi:Doi
964 10.1577/1548-8675(2002)022<0713:Qfdcis>2.0.Co;2.

965 van Genuchten, M. T. (1980), A Closed-form Equation for Predicting the Hydraulic
966 Conductivity of Unsaturated Soils¹, *Soil Science Society of America Journal*, 44(5), 892-898,
967 doi:10.2136/sssaj1980.03615995004400050002x.

968 Waichler, S. R., W. A. Perkins, and M. C. Richmond (2005), Hydrodynamic Simulation of the
969 Columbia River, Hanford Reach, 1940-2004*Rep. PNNL-15226*, Pacific Northwest National
970 Laboratory, Richland, WA.

971 Williams, M. D., M. L. Rockhold, P. D. Thorne, and Y. Chen (2008), Three-Dimensional
972 Groundwater Models of the 300 Area at the Hanford Site, Washington State*Rep. PNNL-17708*,
973 Pacific Northwest National Laboratory, Richland, WA.

974 Wood, E. F., D. P. Lettenmaier, and V. G. Zartarian (1992), A land-surface hydrology
975 parameterization with subgrid variability for general circulation models, *Journal of Geophysical*
976 *Research: Atmospheres*, 97(D3), 2717-2728, doi:10.1029/91JD01786.

977 Xu, X., et al. (2016), A multi-scale comparison of modeled and observed seasonal methane
978 emissions in northern wetlands, *Biogeosciences*, 13(17), 5043-5056, doi:10.5194/bg-13-5043-
979 2016.

980 Zachara, J. M., Chen, X., Murray, C., and Hammond, G. (2016). River stage influences on
981 uranium transport in a hydrologically dynamic groundwater-surface water transition zone, *Water*
982 *Resources Research*, 52, 1568-1590, 10.1002/2015WR018009, 2016.

983 Zeng, X., Zhao, M., and Dickinson, R. E. (1998), Intercomparison of bulk aerodynamic
984 algorithms for the computation of sea surface fluxes using TOGA COARE and TAO data,
985 *Journal of Climate*, 11, 2628-2644, 1998.

986 Zeng, X., Dickinson, R. E., Barlage, M., Dai, Y., Wang, G., and Oleson, K. (2005), Treatment of
987 undercanopy turbulence in land models, *Journal of Climate*, 18, 5086-5094,
988 10.1175/JCLI3595.1.

989 Zeng, X., and Wang, A. (2007), Consistent Parameterization of Roughness Length and
990 Displacement Height for Sparse and Dense Canopies in Land Models, *Journal of*
991 *Hydrometeorology*, 8, 730-737, 10.1175/jhm607.1.

992 Zeng, X., and Decker, M. (2009), Improving the Numerical Solution of Soil Moisture-Based
993 Richards Equation for Land Models with a Deep or Shallow Water Table, *Journal of*
994 *Hydrometeorology*, 10, 308-319, 10.1175/2008JHM1011.1.

995 Zhang, B., J. L. Tang, C. Gao, and H. Zepp (2011), Subsurface lateral flow from hillslope and its
996 contribution to nitrate loading in streams through an agricultural catchment during subtropical
997 rainstorm events, *Hydrol. Earth Syst. Sci.*, 15(10), 3153-3170, doi:10.5194/hess-15-3153-2011.

998 Zhou, T., B. Nijssen, H. L. Gao, and D. P. Lettenmaier (2016), The Contribution of Reservoirs to
999 Global Land Surface Water Storage Variations, *Journal of Hydrometeorology*, 17(1), 309-325,
1000 doi:10.1175/jhm-d-15-0002.1.

1001

1002

1003 **Tables and Figures**

1004

1005 Table 1. Summary of numerical experiments

Experiments	Model	Horizontal Resolution	Lateral flow	River Stage (m)
S_{v2m}	CP v1.0	2m	No	Observed
S_{2m}	CP v1.0	2m	Yes	Observed
S_{10m}	CP v1.0	10m	Yes	Observed
S_{20m}	CP v1.0	20m	Yes	Observed
S_{E2m}	CP v1.0	2m	Yes	Observed +5
S_{E10m}	CP v1.0	10m	Yes	Observed +5
S_{E20m}	CP v1.0	20m	Yes	Observed +5
CLM_{2m}	CLM4.5	2m	No	Not applicable

1006

1007

1008 Table 2. Hydrogeological material properties of Hanford and Ringold materials.

Material	Porosity	Permeability (m ²)	Van Genuchten/Burdine Parameters		
			Res. Sat.	m	alpha
Hanford	0.20	7.387×10^{-9}	0.16	0.34	7.27×10^{-4}
Ringold	0.40	1.055×10^{-12}	0.13	0.75	1.43×10^{-4}

1009

1010

1011 Table 3. The comparison between simulated and observed water table levels

Well number	S _{2m}		S _{10m}		S _{20m}	
	RMSE (m)	N-S	RMSE (m)	N-S	RMSE (m)	N-S
399-3-29	0.022	0.999	0.022	0.999	0.021	0.999
399-3-34	0.011	1.000	0.011	1.000	0.006	1.000
399-2-01	0.039	0.997	0.038	0.997	0.029	0.998
399-1-60	0.016	1.000	0.016	0.999	0.013	1.000
399-2-33	0.028	0.998	0.028	0.998	0.022	0.999
399-1-21A	0.023	0.999	0.023	0.999	0.020	0.999
399-2-03	0.037	0.997	0.037	0.997	0.029	0.998
399-2-02	0.045	0.995	0.045	0.995	0.042	0.996
mean	0.028	0.998	0.028	0.998	0.023	0.999

1012

1013

1014 Table 4. The relative error in surface energy fluxes simulated by S_{10m} and S_{20m} benchmarked against
1015 S_{2m} and by S_{E10m} and S_{E20m} benchmarked against S_{E2m}

<i>Simulation</i>	<i>Latent heat flux (%)</i>	<i>Sensible heat flux (%)</i>
S_{v2m}	5.67	1.63
S_{10m}	1.35	0.78
S_{20m}	2.41	1.42
S_{E10m}	33.19	13.71
S_{E20m}	33.84	14.18

1016

1017

1018 Table 5. The relative error in total water mass and tracer amount in the subsurface simulated in S_{10m} and
1019 S_{20m} benchmarked against S_{2m} and by S_{E10m} and S_{E20m} benchmarked against S_{E2m}

<i>Simulation</i>	Total water mass (%)	Total tracer (%)
S_{10m}	0.03	5.44
S_{20m}	0.04	10.40
S_{E10m}	9.87	22.00
S_{E20m}	9.85	22.00

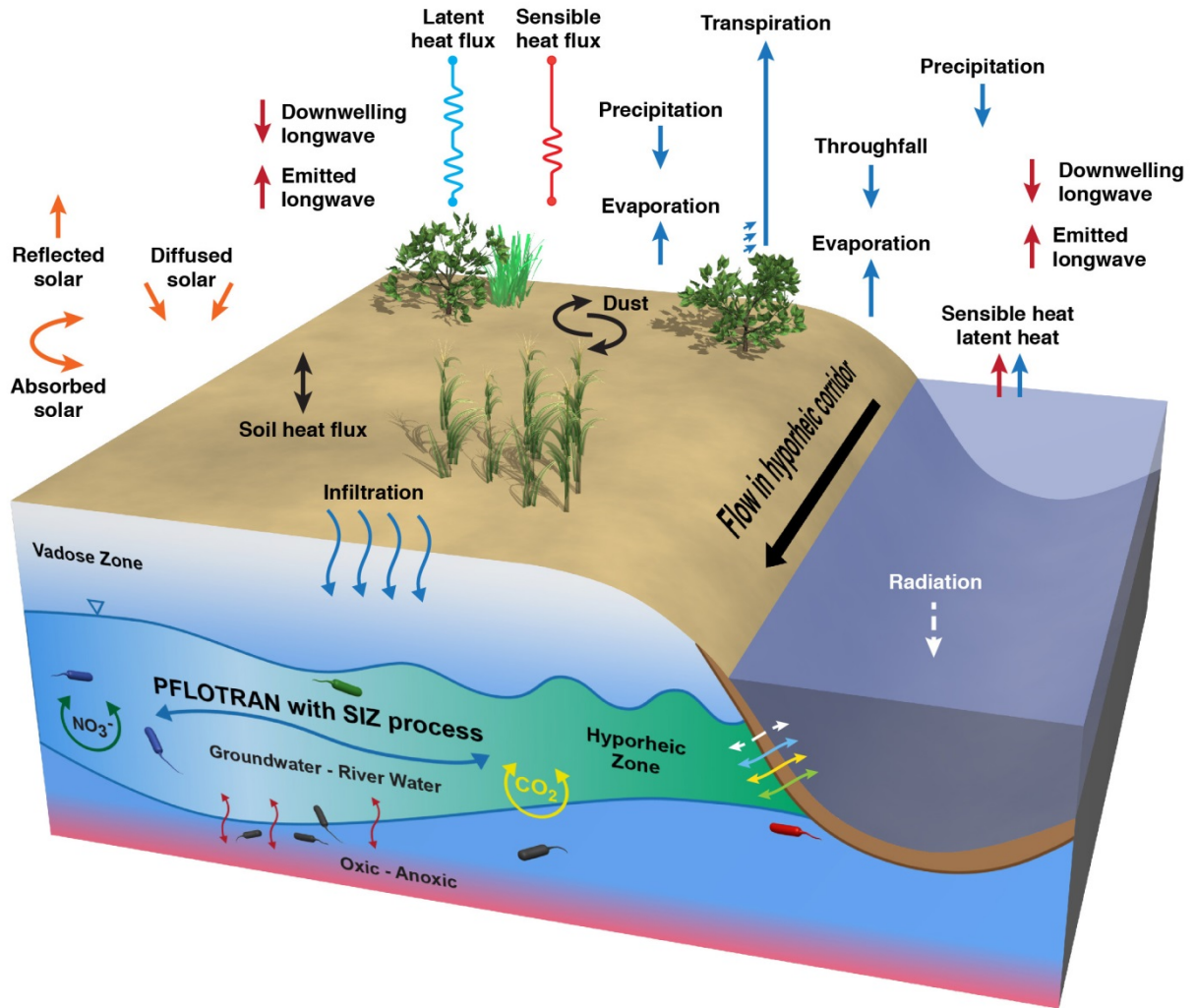
1020

1021

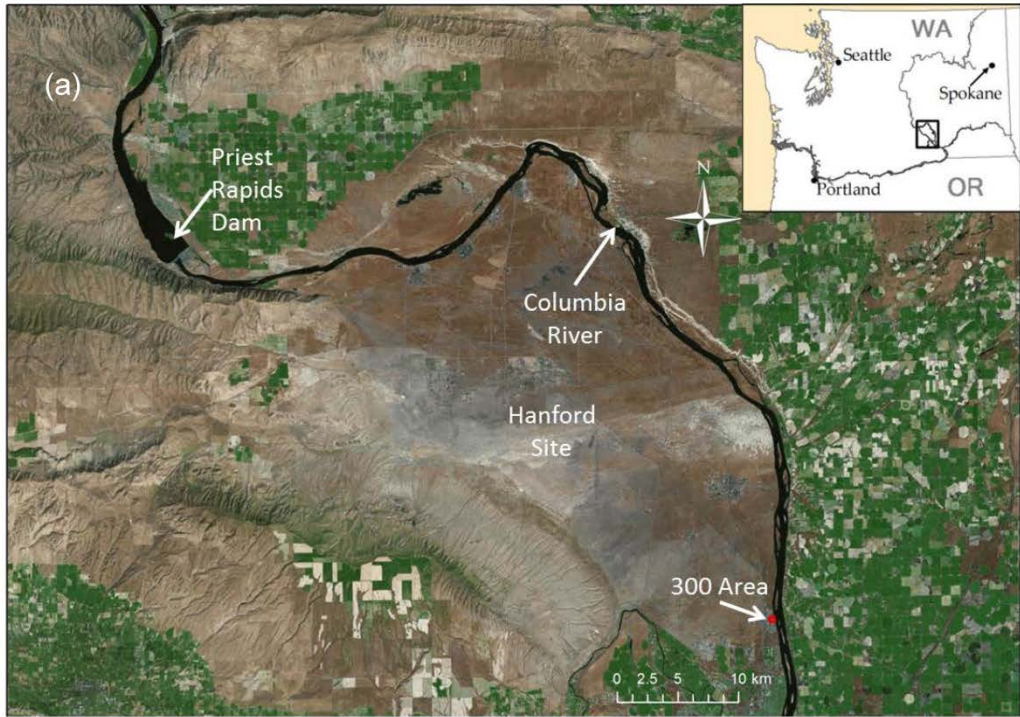


1022
 1023
 1024
 1025
 1026
 1027
 1028
 1029

Figure 1. Schematic representations of the model coupling interface of CP v1.0. (a) Domain decomposition of a hypothetical CLM and PFLOTRAN domain comprising of 4x1x7 and 4x1x5 grids in x, y, and z directions across two processors as shown in blue and green. (b) Mapping of water fluxes from CLM onto PFLOTRAN domain via a local sparse matrix vector product for grids on processor 1. (c) Mapping of updated soil moisture from PFLOTRAN onto CLM domain via a local sparse matrix vector product for grids on processor 1.

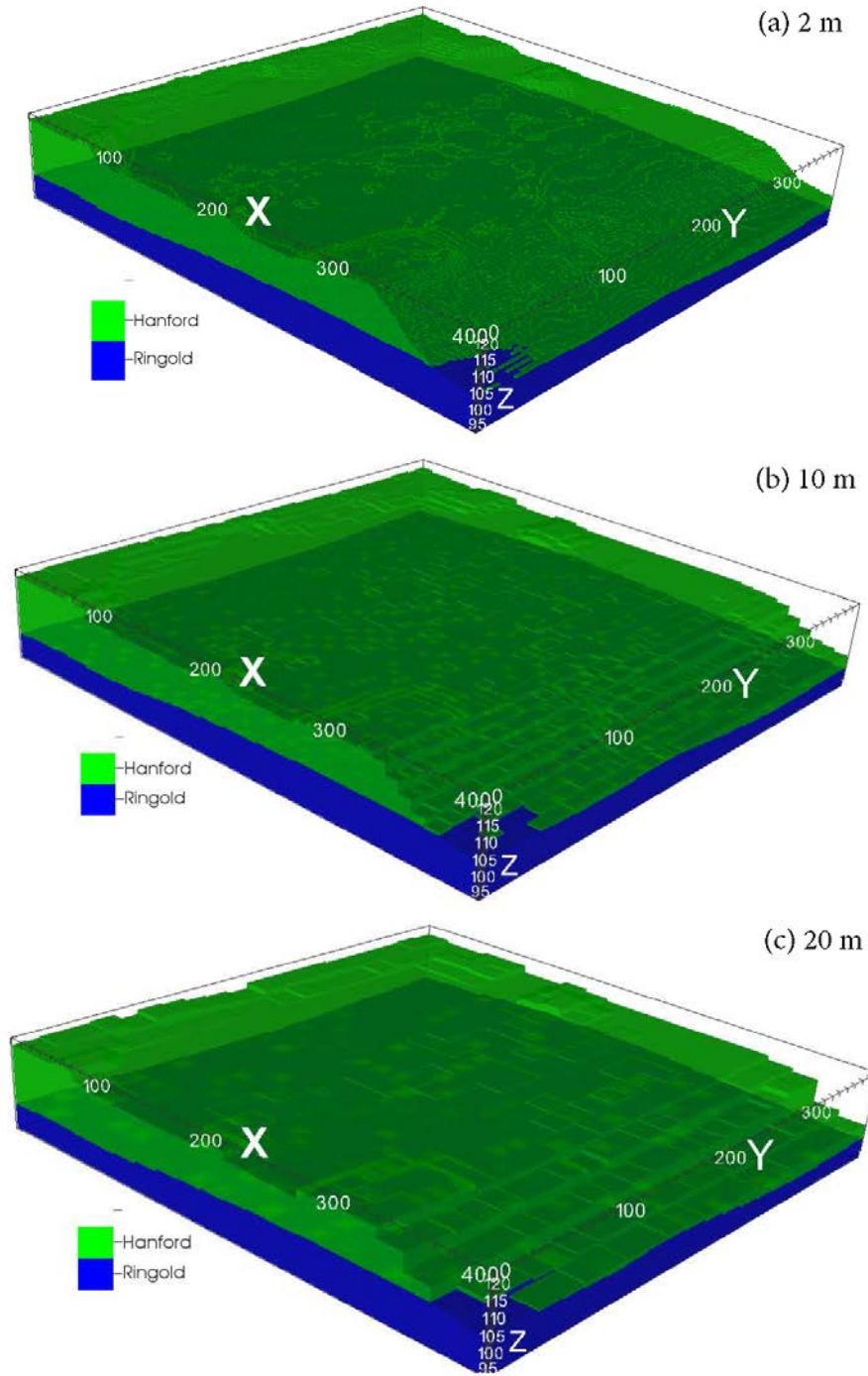


1030
 1031 Figure 2. Schematic representation of hydrologic processes simulated in CP v1.0



1032

1033 Figure 3. (a) The Hanford Reach of the Columbia River and the Hanford Site location in south-central
 1034 Washington State, USA; (b) the 400 m x 400 m modeling domain located in the Hanford 300 Area.

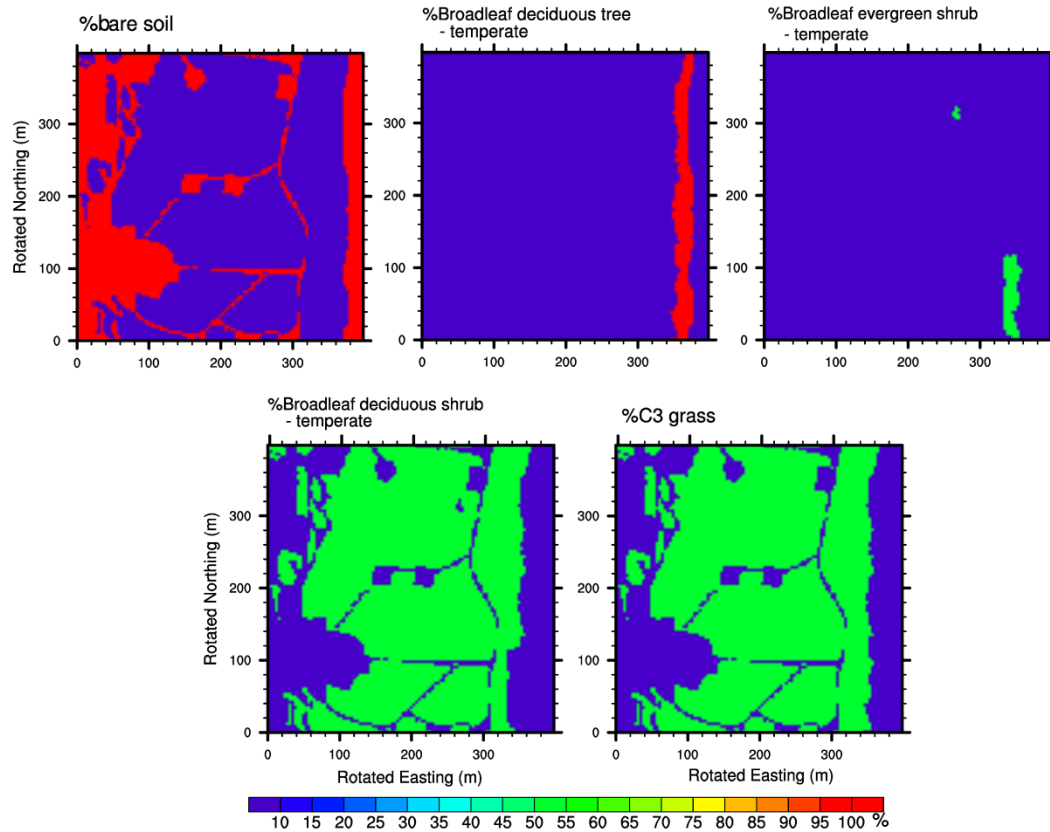


1035

1036 Figure 4. PFLOTRAN meshes and associated material IDs at (a) 2-m; (b) 10-m; and (c) 20-m resolutions

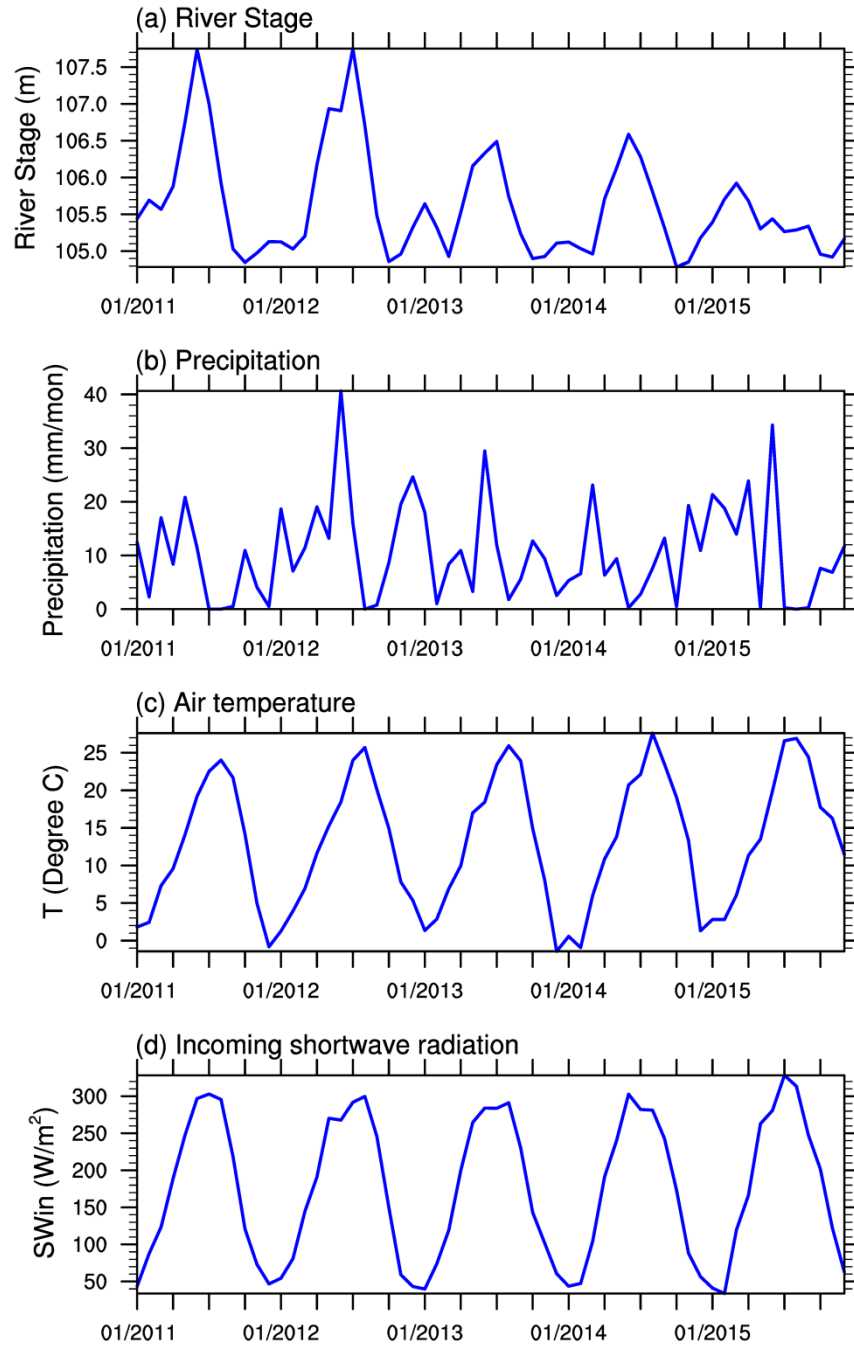
1037

1038



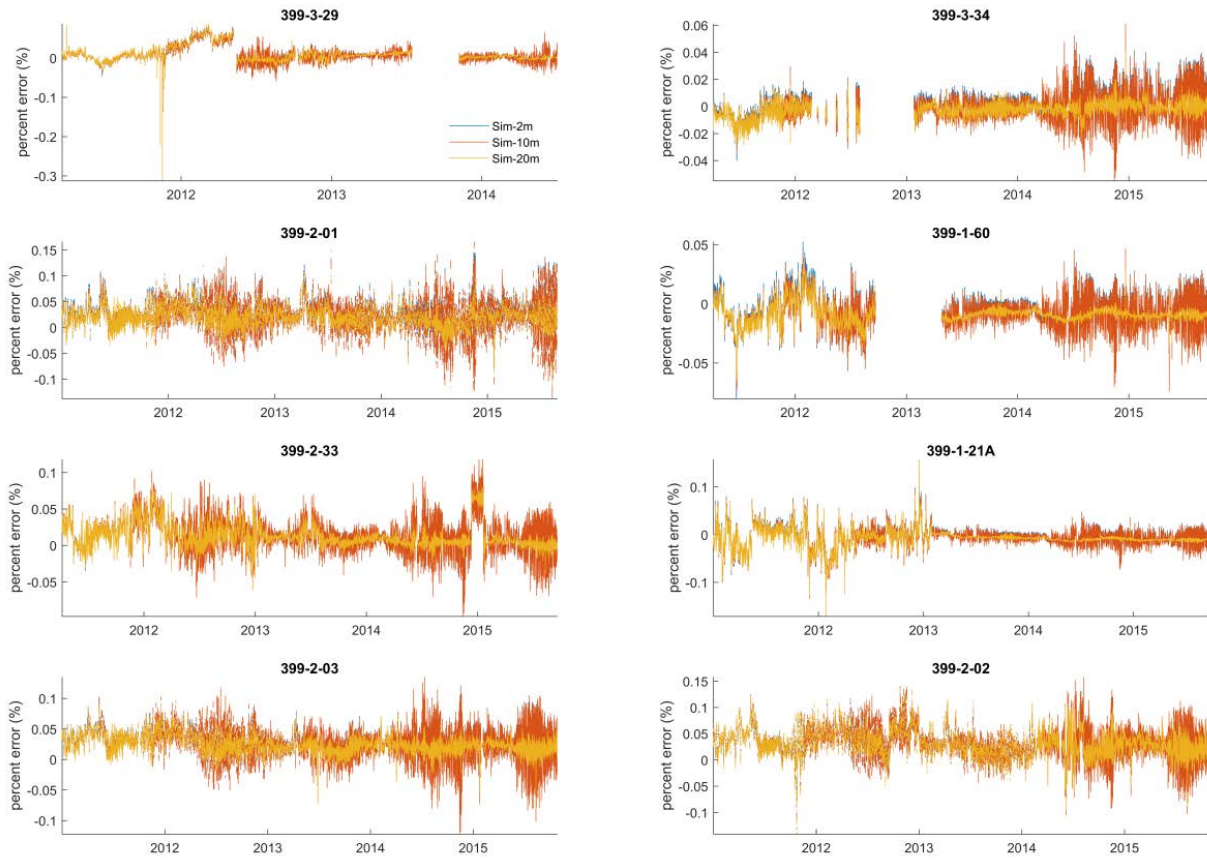
1039

1040 Figure 5. Plant function types at 2-m resolution as inputs for CLM4.5



1041

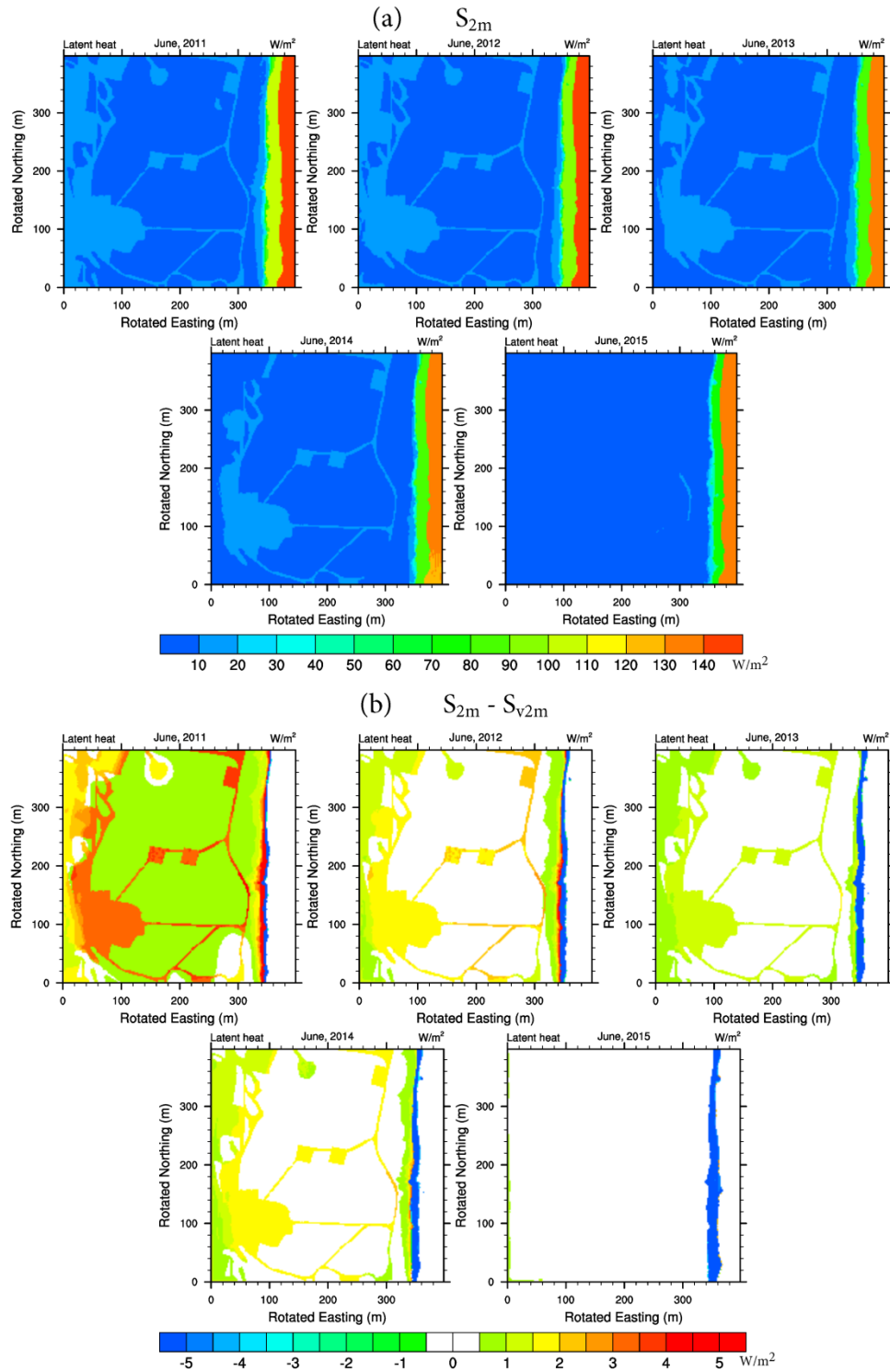
1042 Figure 6. Hydro-meteorological drivers in the study period: (a) monthly mean river Stage; (b) monthly
 1043 total precipitation; (c) monthly mean surface air temperature; (d) and monthly mean incoming shortwave
 1044 radiation.



1045

1046 Figure 7. Deviation (in percentages) of simulated water table levels from observations at selected wells
 1047 shown in Figure 3b.

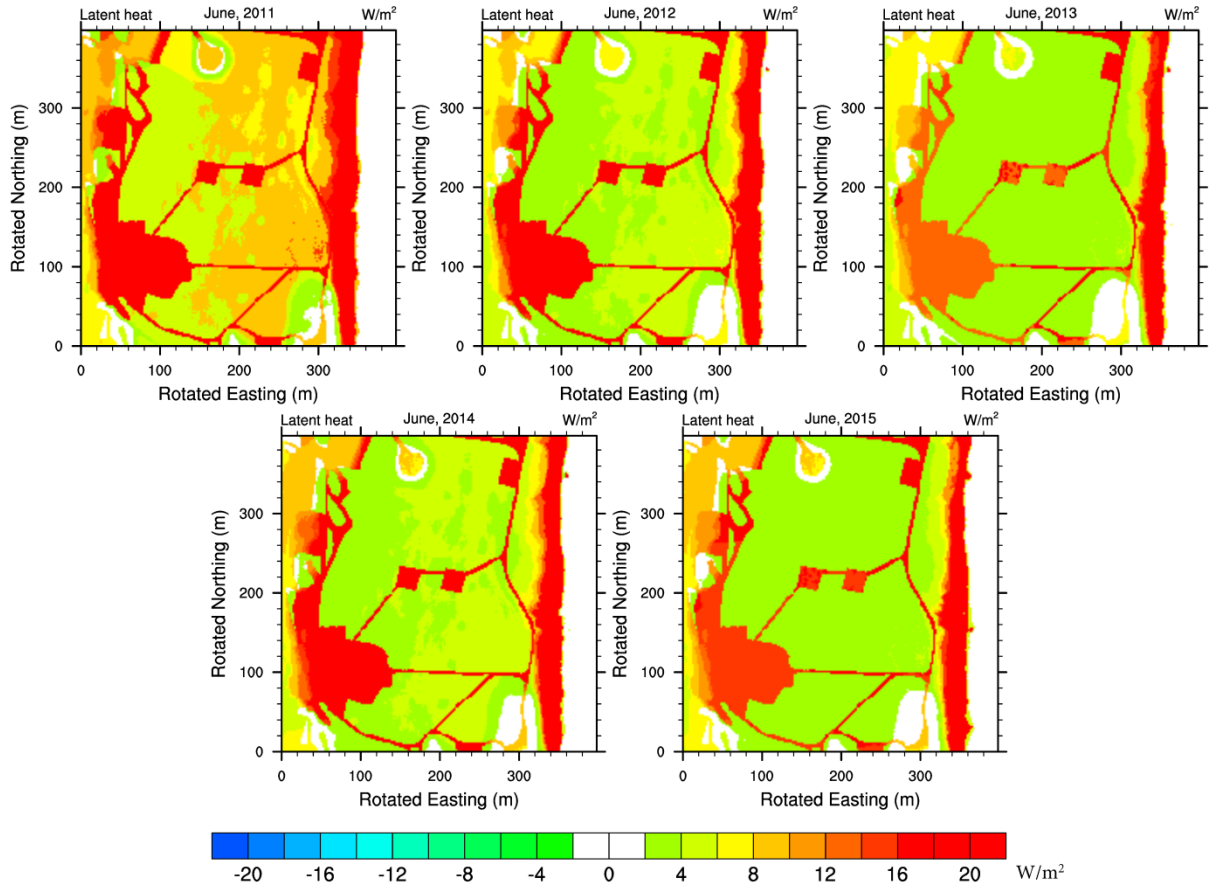
1048



1049

1050 Figure 8. (a) Simulated latent heat fluxes in June from the 3-D simulation (S_{2m}); and (b) the difference
 1051 between the 3-D and vertical only simulations (i.e., $S_{2m} - S_{v2m}$).

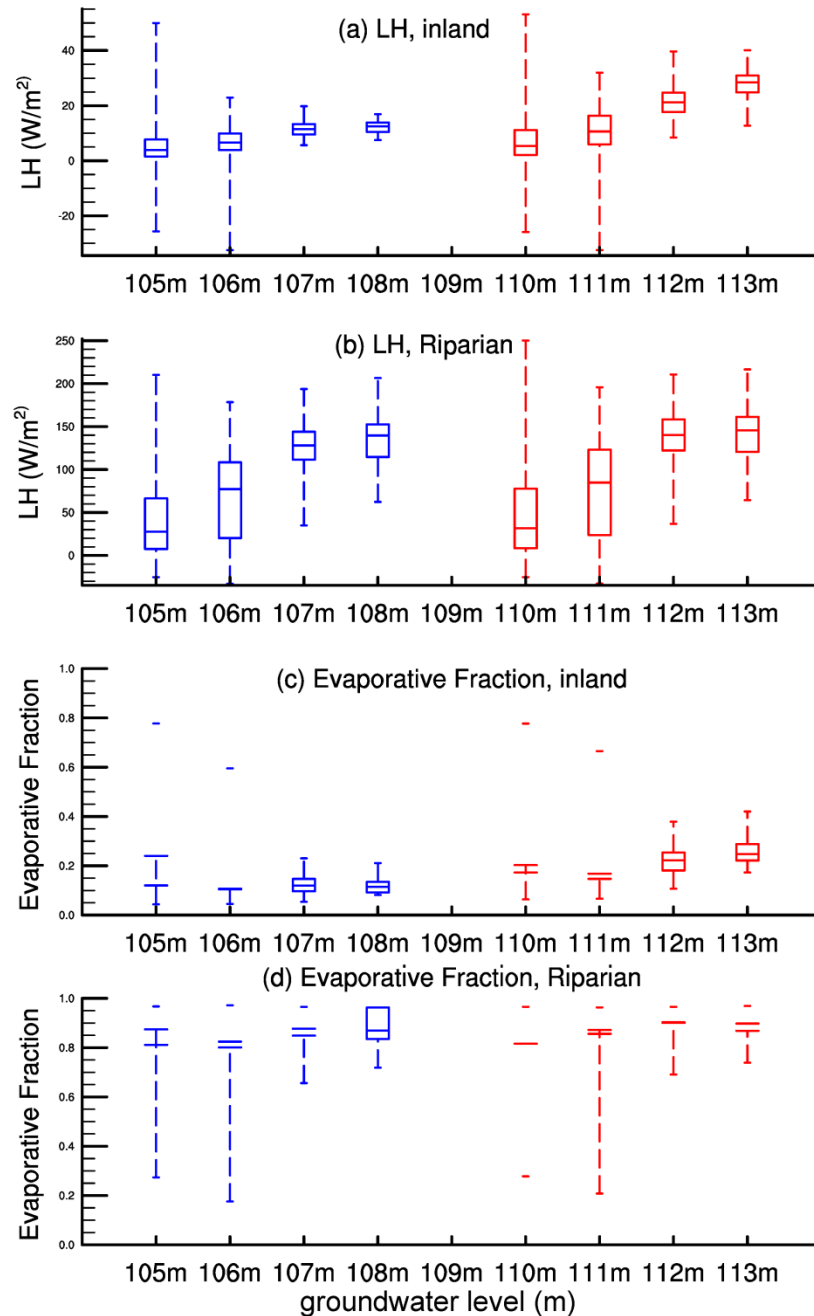
1052



1053

1054 Figure 9. Difference between simulated latent heat fluxes by S_{E2m} and S_{2m} in June.

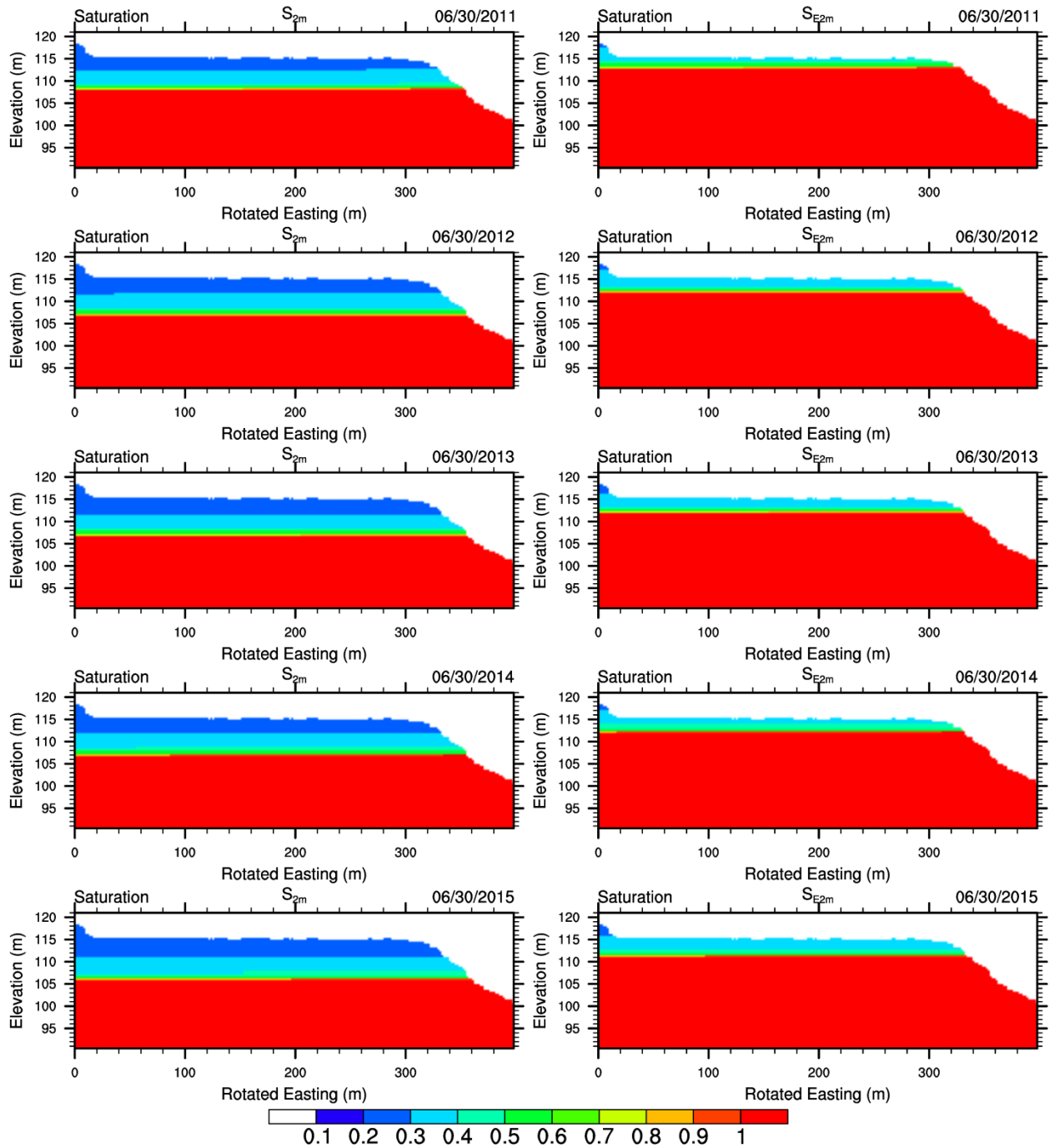
1055



1056

1057 Figure 10. Boxplots of (a) land heat fluxes over the inland domain; (b) and latent heat fluxes in the
 1058 riparian zone; (c) Evaporative fractions over the inland domain; (d) Evaporative fractions in the riparian
 1059 zone in relation to groundwater table levels in the five-year period. The red boxes and whiskers represent
 1060 summary statistics from S_{2m} , and red ones indicate those from S_{E2m} . The bottom and top of each box are
 1061 the 25th and 75th percentile, the band inside the box is median, and the ends of the whiskers are
 1062 maximum and minimum values, respectively.

Transect, y=200m

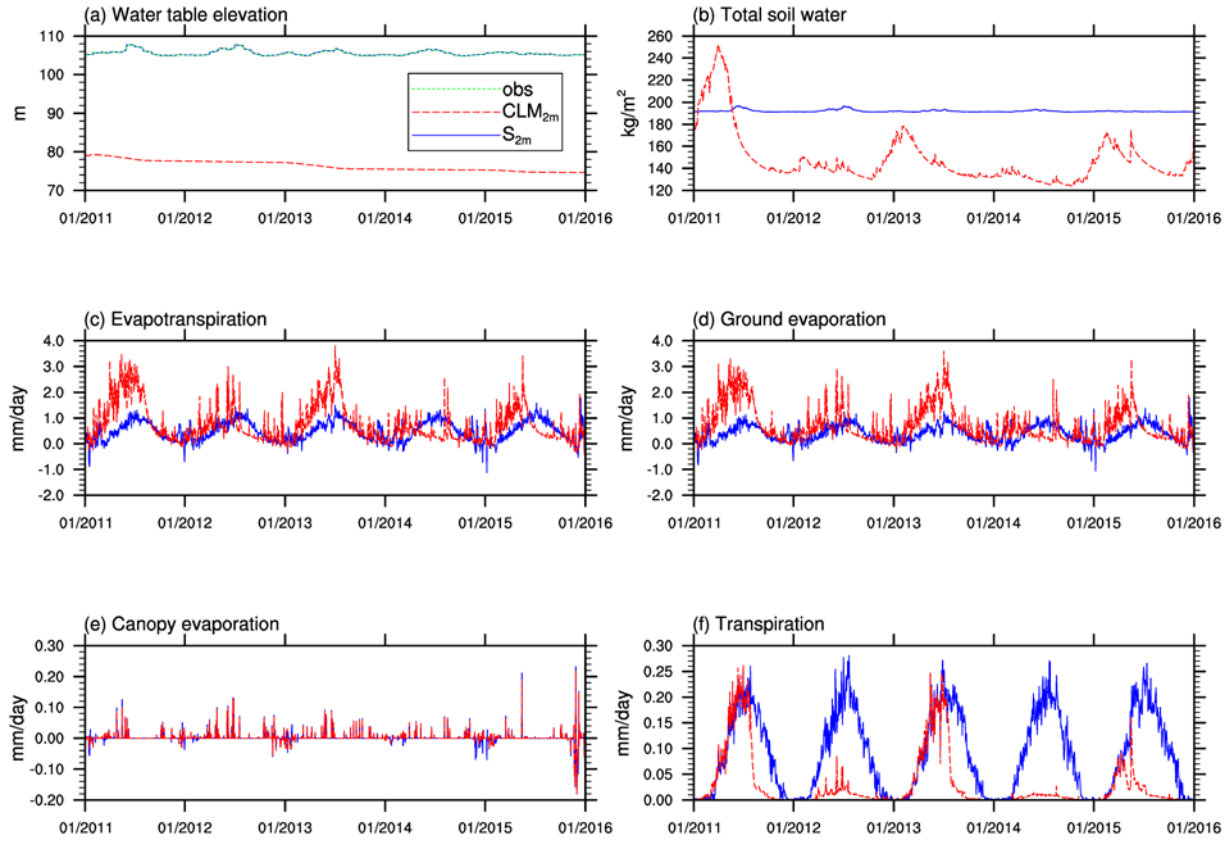


1063

1064 Figure 11. Liquid saturation levels (unitless) across a transect perpendicular to the river ($y=200m$) on 30

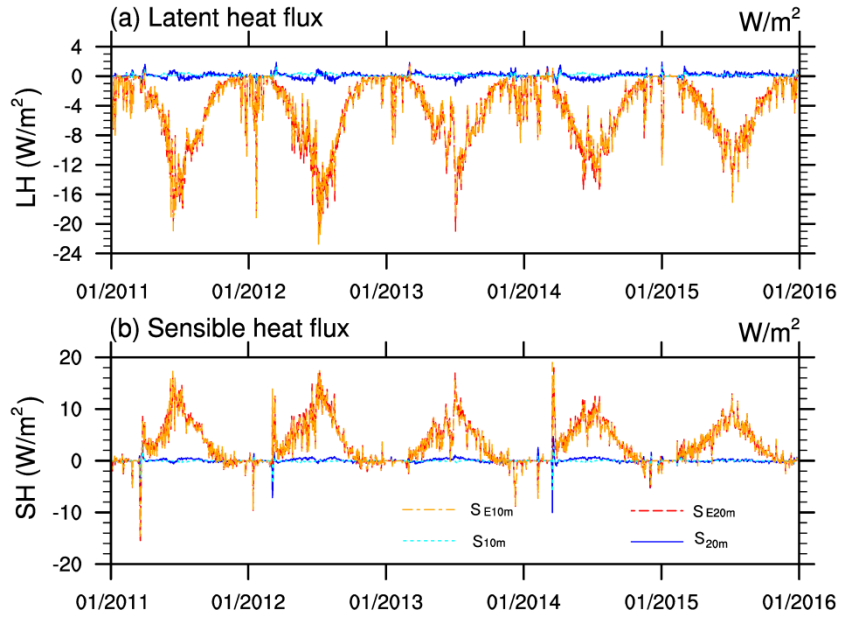
1065 June of each year in the study period from (a) S_{2m} and (b) S_{E2m} .

1066



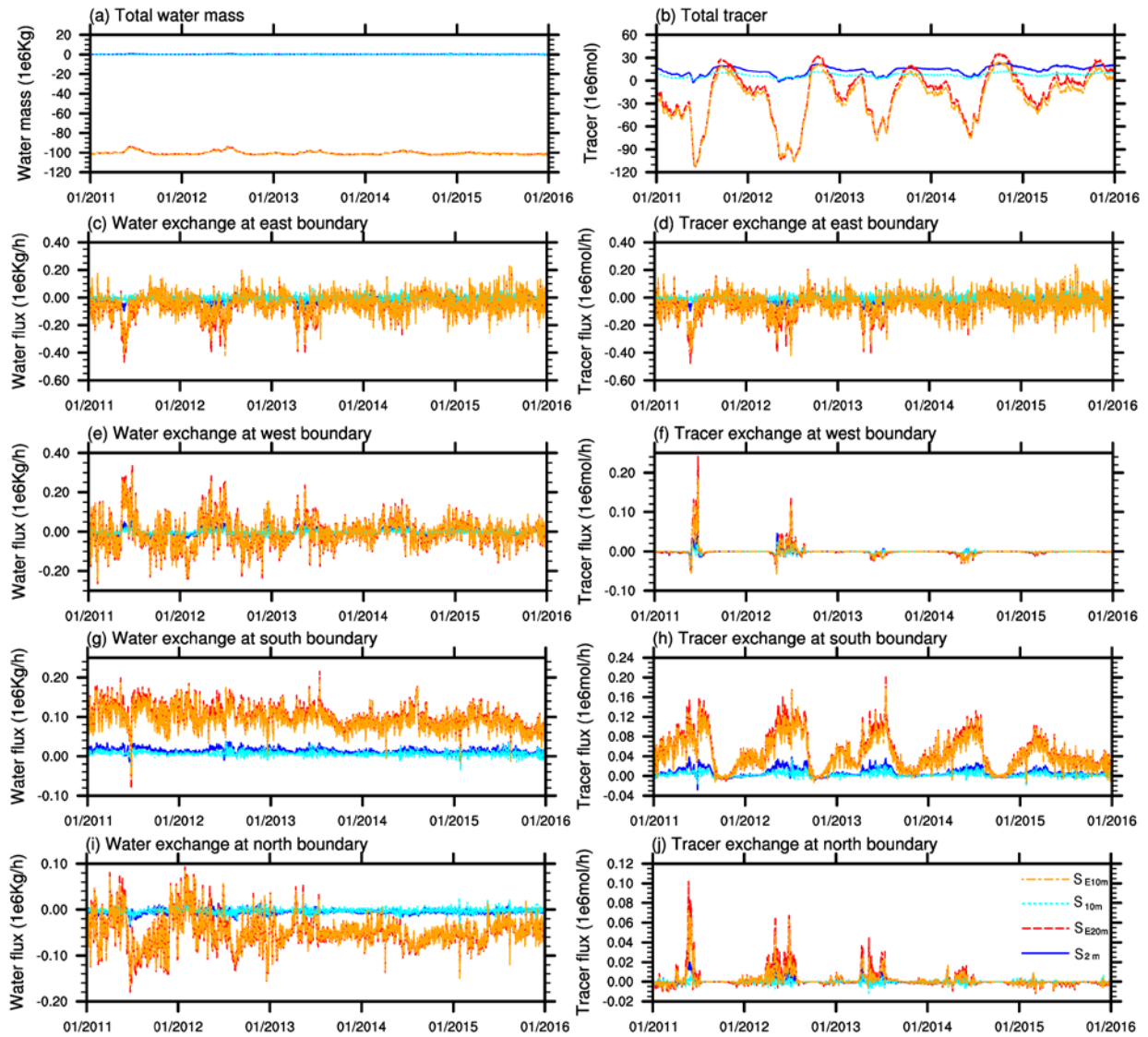
1067
1068

Figure 12. Comparison of key hydrologic fluxes and state variables simulated by CLM_{2m} and S_{2m}.



1069

1070 Figure 13. Deviations of simulated domain-average latent heat and sensible heat fluxes from those
 1071 simulated by S_{2m} (for S_{10m} and S_{20m}), and by S_{E2m} (for S_{E10m} and S_{E20m}).



1072
 1073 Figure 14. Deviations of total water mass, tracer, and exchange rates of water and tracer at four
 1074 boundaries from those simulated by S_{2m} (for S_{10m} and S_{20m}), and by S_{E2m} (for S_{E10m} and S_{E20m}).

1075